



# Exploring bias in the OCO-3 snapshot area mapping mode via geometry, surface, and aerosol effects

Emily Bell<sup>1</sup>, Christopher W. O'Dell<sup>1</sup>, Thomas E. Taylor<sup>1</sup>, Aronne Merrelli<sup>2</sup>, Robert R. Nelson<sup>3</sup>, Matthäus Kiel<sup>3</sup>, Annmarie Eldering<sup>3</sup>, Robert Rosenberg<sup>3</sup>, and Brendan Fisher<sup>3</sup>

<sup>1</sup>Cooperative Institute for Research in the Atmosphere, Colorado State University, Fort Collins, CO 80521, USA

<sup>2</sup>Department of Climate and Space Sciences and Engineering, University of Michigan, Ann Arbor, MI 48109, USA

<sup>3</sup>Jet Propulsion Laboratory, California Institute of Technology, Pasadena, CA 91109, USA

**Correspondence:** Emily Bell (embell@colostate.edu)

Received: 17 August 2022 – Discussion started: 26 August 2022

Revised: 19 November 2022 – Accepted: 24 November 2022 – Published: 12 January 2023

**Abstract.** The Atmospheric Carbon Observations from Space (ACOS) retrieval algorithm has been delivering operational column-averaged carbon dioxide dry-air mole fraction ( $X_{\text{CO}_2}$ ) data for the Orbiting Carbon Observatory (OCO) missions since 2014. The ACOS Level 2 Full Physics (L2FP) algorithm retrieves a number of parameters, including aerosol and surface properties, in addition to atmospheric  $\text{CO}_2$ . Past analysis has shown that while the ACOS retrieval meets mission precision requirements of 0.1 %–0.5 % in  $X_{\text{CO}_2}$ , residual biases and some sources of error remain unaccounted for (Wunch et al., 2017; Worden et al., 2017; Torres et al., 2019). Forward model and other errors can lead to systematic biases in the retrieved  $X_{\text{CO}_2}$ , which are often correlated with these additional retrieved parameters. The characterization of such biases is particularly essential to urban- and local-scale emissions studies, where it is critical to accurately distinguish source signals relative to background concentrations (Nassar et al., 2017; Kiel et al., 2021). In this study we explore algorithm-induced biases through the use of simulated OCO-3 snapshot area mapping (SAM) mode observations, which offer a unique window into these biases with their wide range of viewing geometries over a given scene. We focus on a small percentage of SAMs in the OCO-3 vEarly product which contains artificially strong across-swath  $X_{\text{CO}_2}$  biases spanning several parts per million, related to observation geometry. We investigate the causes of swath bias by using the timing and geometry of real OCO-3 SAMs to retrieve  $X_{\text{CO}_2}$  from custom simulated Level 1b radiance spectra. By building relatively simple scenes and testing a variety of parameters, we find that aerosol is the primary

driver of swath bias, with a complex combination of viewing geometry and aerosol optical properties contributing to the strength and pattern of the bias. Finally, we seek to understand successful mitigation of swath bias in the new OCO-3 version 10 data product. Results of this study may be useful in uncovering other remaining sources of  $X_{\text{CO}_2}$  bias and may help minimize similar retrieval biases for both present missions (GOSAT, GOSAT-2, OCO-2, OCO-3, TanSat) and future missions (e.g., MicroCarb, GeoCarb, GOSAT-GW, CO2M).

## 1 Introduction

With the human-induced warming of Earth's climate system well underway, the study of anthropogenic greenhouse gas emissions – and in particular, carbon dioxide ( $\text{CO}_2$ ) – plays a major role in the development of both local and international climate policy. A robust understanding of Earth's carbon cycle, including both natural and anthropogenic contributions, is essential, and involves a myriad of challenges. Since the launch of the SCanning Imaging Absorption spectroMeter for Atmospheric CHartography (SCIAMACHY; Bovensmann et al., 1999) in 2002 aboard the European Space Agency's Envisat, space-based instruments have been addressing the particular challenge of scale: in decades prior, the global carbon cycle was studied using a handful of highly localized ground measurements scattered across, mostly, the Northern Hemisphere land surface; SCIAMACHY and its successors have changed this limitation profoundly (Buch-

witz et al., 2007; Schneising et al., 2008). The Greenhouse gases Observing SATellite (GOSAT; Kuze et al., 2009; Yokota et al., 2009), launched in 2009, as well as the Orbiting Carbon Observatory missions (OCO-2 and OCO-3), both launched in the 2010s, have improved upon SCIAMACHY's ability to measure CO<sub>2</sub> over a large fraction of Earth's surface, with more continuous spatial coverage than ground-based networks can provide. With their increasingly fine spatial resolution, precision, and accuracy, space-based observations from the OCO missions can now resolve carbon sources around the globe on scales as fine as those of individual power plant plumes (Nassar et al., 2017; Reuter et al., 2019).

OCO-3, a three-band grating spectrometer that measures reflected sunlight in the near infrared, was launched in 2019 and is mounted on board the International Space Station (ISS). It observes Earth's atmosphere in eight across-swath footprints, measuring roughly 1.6 by 2.2 km<sup>2</sup> on the ground. Just like its precursor OCO-2, it targets column-averaged carbon dioxide ( $X_{\text{CO}_2}$ ) with spectral measurements of reflected sunlight in three bands: the oxygen A-band (O<sub>2</sub> A-band) at 0.76 μm, a weakly absorbing ("weak") CO<sub>2</sub> band at 1.61 μm, and a more strongly absorbing ("strong") CO<sub>2</sub> band at 2.06 μm (Taylor et al., 2020). Best estimates of  $X_{\text{CO}_2}$  are calculated via an optimal estimation method (Rodgers, 2000), using the Atmospheric Carbon Observations from Space (ACOS) Level 2 Full Physics (L2FP) retrieval algorithm, which has been shown to achieve OCO-2 mission precision requirements of 0.1 %–0.5 % (Wunch et al., 2017; O'Dell et al., 2018). Operational data include a binary quality flag that uses several variables potentially indicative of compromised data fidelity – including aerosol optical depths (AODs), retrieved surface albedo, surface roughness, and differences from model estimates – to filter out "lesser quality" soundings (Osterman et al., 2020). An empirical bias correction is also included with operational datasets, which includes a footprint bias correction, a parametric bias correction, and a global scaling factor – all of which act to mitigate systematic biases within the ACOS retrieved  $X_{\text{CO}_2}$  (O'Dell et al., 2018).

Of particular use in the analysis of fine-scale carbon emission estimates are the OCO-2 and 3's target and OCO-3's snapshot area mapping (SAM) mode measurements. In target and SAM modes, the instrument points at a specific off-nadir location and scans multiple times during an overpass, in an effort to produce a data-dense, spatially coherent map of  $X_{\text{CO}_2}$ . Details of these observation modes will be discussed in the next section. These measurements are the first of their kind to target urban- and local-scale emissions, such as those from megacities or individual power plants. Figure 1 provides an example of a visible  $X_{\text{CO}_2}$  enhancement (or, rather, two areas of enhanced  $X_{\text{CO}_2}$ ) over a power plant site, as seen by OCO-3. In this case, the enhancement extends to the northeast across four OCO-3 swaths, which we define as individual along-track scans. Each swath is eight footprints wide – these are visualized in the right-hand panel as white

rectangles. Point source signals are difficult to quantify, because the instrument noise is a similar order of magnitude to the  $X_{\text{CO}_2}$  enhancement; the  $X_{\text{CO}_2}$  enhancement is also often 2 orders of magnitude smaller than the background concentration. Nitrogen dioxide (NO<sub>2</sub>), co-emitted with CO<sub>2</sub> in fossil fuel combustion, is a helpful validation source for fossil signals due to NO<sub>2</sub>'s short lifetime and high concentration relative to background values. Indeed, co-located NO<sub>2</sub> observations have been shown to be helpful in plume identification when using OCO-2 data (Reuter et al., 2019). We show observations from the Tropospheric Monitoring Instrument (TROPOMI) NO<sub>2</sub> product (Veefkind et al., 2012; Van Geffen et al., 2019) in the right-hand panel of Fig. 1. Because the OCO-3  $X_{\text{CO}_2}$  and TROPOMI NO<sub>2</sub> observations compare so well, we believe the  $X_{\text{CO}_2}$  enhancement to be a real feature of the atmospheric state in this scene.

A clear distinction between  $X_{\text{CO}_2}$  enhancement and background is critical and can be easily complicated by retrieval biases stemming from a variety of factors. Through small-area analysis of OCO-2 target data, it is well known that estimates of  $X_{\text{CO}_2}$  from the ACOS L2FP retrieval algorithm have errors dependent on aerosol and clouds within the field of view, variations in the surface reflectances and bi-directional reflectance distribution functions (BRDF), and viewing and solar geometries (Wunch et al., 2017; Worden et al., 2017; Torres et al., 2019). Target and SAM mode measurements are especially helpful for evaluating geometry-related effects, as they take a large number of measurements (typically several thousand soundings) over less than a 2 min time period: they sample a near-constant atmospheric state, leaving the changing geometry as the primary independent variable. Thus, in both targets and SAMs, we expect any spatially coherent biases to be primarily due to the retrieval's imperfect treatment of the effects of changing solar and observation geometry or changes in surface albedo within the scene.

SAM measurements are novel in their spatial coverage, specific to OCO-3, and are a valuable resource in studying geometry-related effects. In fact, the OCO-3 vEarly dataset – the first publicly released OCO-3 L2FP product – provides a striking operational example of geometry-dependent biases in a small fraction of SAM cases. In these SAMs, we observe a highly unphysical  $X_{\text{CO}_2}$  gradient of several parts per million (ppm) in the across-swath direction, often with a step-wise increase from swath to swath: Fig. 2 provides two examples. We refer to this phenomenon as swath bias. Swath bias was found in multiple SAMs each month throughout vEarly data processing and appeared to occur more frequently over sites with high surface albedo and scenes with high AODs. The swath bias is also regularly seen over urban sites, and the  $X_{\text{CO}_2}$  gradient in these cases often meets or exceeds the average 1–5 ppm enhancement we expect from fossil fuel signals. This can make the differentiation between bias and real signal quite challenging and renders these SAM data less usable for emissions studies; thus, the magnitude, prevalence, and importance of OCO-3 swath bias SAMs make them an in-

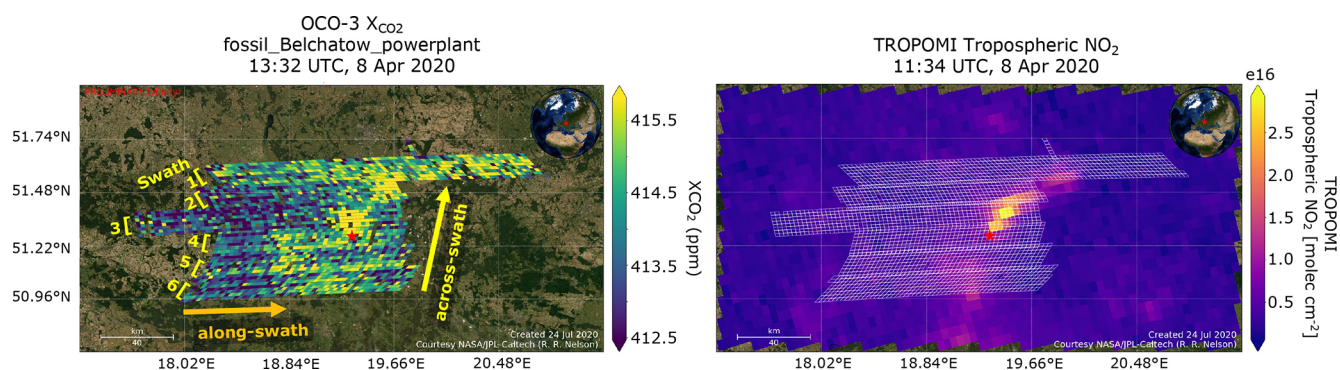


**Figure 1.** OCO-3 vEarly SAM showing observed  $X_{\text{CO}_2}$  enhancements compared to coincident TROPOMI  $\text{NO}_2$  data over the Belchatow power station in Poland. We have identified individual swaths using brackets; the along-swath and across-swath dimensions, which we will refer to repeatedly in this work, are designated by the colored arrows.

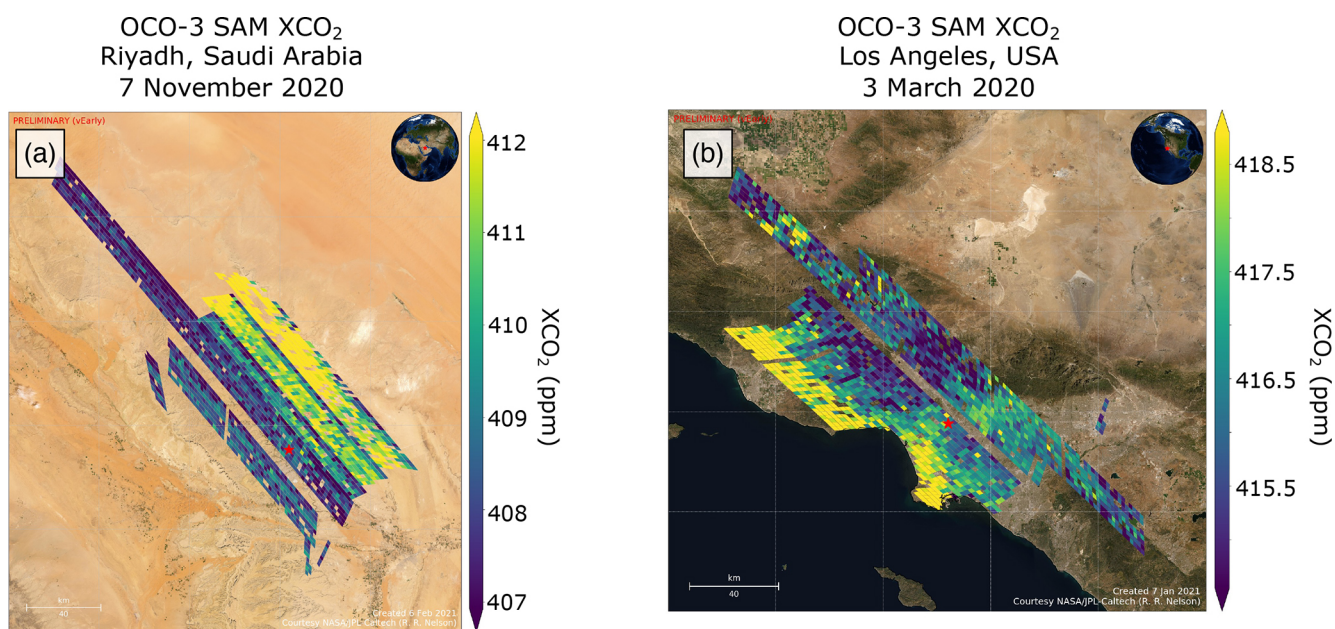


**Figure 2.** Two examples of swath bias from the raw (no filtering or bias correction) OCO-3 vEarly  $X_{\text{CO}_2}$  data product, over (a) Riyadh, Saudi Arabia, and (b) Los Angeles, USA.

triguing source of study. Future missions with similar GHG-monitoring strategies, such as MicroCarb (Pasternak et al., 2017; Bertaux et al., 2020), GeoCarb (Moore et al., 2018; Nivitanont et al., 2019), GOSAT-GW (Kasahara et al., 2020), and CO2M (Ciais et al., 2017; Janssens-Maenhout et al., 2020), may benefit from an improved understanding of these types of biases.

In Sect. 2, we review the similarities and differences between OCO-3 target and SAM mode measurements. Section 3 focuses on the swath bias (shorthand “SB”) in the OCO-3 vEarly dataset, where we have created a set of criteria to identify an SB pattern in any given vEarly SAM. We identify SB in approximately 12 % of vEarly SAMs and identify potential systematic behavioral differences between

those 12 % of L2FP retrievals and the rest of the dataset. Optical path length, AOD, and surface albedo arise as particular variables of interest.

Simulation-based studies, such as O’Dell et al. (2012), are useful for identifying major sources of error in retrievals, such as those due to aerosol, clouds, or surface effects. They can also help to identify cause and effect rather than pure correlation. We therefore pursue a simulation-based approach to help identify the root causes of swath bias relative to the hypotheses we form in Sect. 2. We employ the L1b simulator (O’Brien et al., 2009) and the ACOS L2FP retrieval algorithm (O’Dell et al., 2012, 2018) to test those behaviors. In Sect. 4, we describe our simulations of OCO-3 SAM mode data, starting from time and geometry information col-

lected on orbit. Semi-realistic scenes are built using information from the National Centers for Environmental Prediction (NCEP; Kalnay et al., 1996) model (meteorology and trace gases), CarbonTracker's CT2019B (CO<sub>2</sub>; Jacobson et al., 2020), Cloud-Aerosol Lidar with Orthogonal Polarization (CALIOP, vertical aerosol number concentrations; Winker et al., 2007), and Moderate Resolution Imaging Spectroradiometer (MODIS, surface albedo, and BRDF parameters; Schaaf and Wang, 2015). We keep surface and aerosol setups relatively simple to isolate the effects of changing viewing geometry. We provide a brief overview of the ACOS retrieval algorithm in Sect. 5. Section 6 discusses the results of our full simulation experiments, from the generation of L1b spectra to the final retrieved L2FP  $X_{\text{CO}_2}$  concentration. We initially attempt to replicate the observed SB in a few notable SAMs and then focus on a set of three cases over one site. We manipulate different scene inputs – aerosol optical depth, type, and height, plus surface albedo – to evaluate their effect on the resulting simulated  $X_{\text{CO}_2}$  patterns.

Finally, in Sect. 7 we seek to explain why the SB is significantly mitigated in the OCO-3 version 10 data product compared to vEarly. Ultimately, we hope that an improved understanding of the SB, summarized in Sect. 8, can prevent similar biases in future CO<sub>2</sub> monitoring missions.

## 2 OCO target and SAM mode measurements

Both OCO-2 (Crisp et al., 2017; Eldering et al., 2017) and OCO-3 (Basilio et al., 2019; Eldering et al., 2019; Taylor et al., 2020) are well-documented missions in the literature; finer details on instrumentation and global datasets will be left to other publications. Of specific importance to this work are the aforementioned OCO-3 SAM mode measurements, a successor to OCO-2's target mode. Target mode was developed for OCO-2 to scan a small area continuously in an overlapping pattern as the satellite passes overhead. On OCO-2, this continuous scanning is achieved by changing the orientation, and thus viewing angle, of the satellite itself, through a series of complex maneuvers in orbit. The pointing method of OCO-3, however, is mechanically different, due to its fixed-mount position on board the International Space Station (ISS). Rather than adjust the physical orientation of the instrument itself, OCO-3 is outfitted with a 2-D pointing mirror assembly (PMA), which provides the ability to scan larger areas during a single overpass. This broader scan defines OCO-3's SAM mode. A typical SAM spans a ground area of about  $80 \times 80$  km ( $1600$  km<sup>2</sup>), and each of the approximately five scans, or swaths, are adjacent to one another, rather than overlapping, to create a larger spatial "map" of  $X_{\text{CO}_2}$  than OCO-2 target mode. OCO-3 has recorded more than 7000 SAMs between August 2019 and June 2022. The OCO-3 SAM site list includes volcanoes, cities, power plants, and occasionally other scientific points of interest, such as flight campaigns or ground-based tow-

ers. Figure 3 gives a side-by-side example of an OCO-2 target versus an OCO-3 SAM over Los Angeles, taken 2 years apart; Fig. 4 illustrates the diversity of OCO-3 SAM and target sites observed from launch to July 2022.

OCO-2 target mode is primarily used for validation purposes, with many targets located at Total Column Carbon Observing Network (TCCON; Wunch et al., 2011) sites, but it also includes targets over certain megacities and some point sources, such as volcanoes and large power plants. OCO-3's target mode is utilized similarly but has a larger spatial coverage, which can also be used to study the carbon cycle on local scales (Kiel et al., 2021; Reißmann et al., 2022). Studies using OCO-2 target data have shown the instrument's ability to detect anthropogenic  $X_{\text{CO}_2}$  enhancements on subcontinental scales (Hakkariainen et al., 2016), from megacities (Schwandner et al., 2017) and from industrial sources such as iron and steel plants (Wang et al., 2018). Nassar et al. (2017) even used OCO-2 nadir and glint observations fitted to a Gaussian plume model to quantify CO<sub>2</sub> emissions from seven coal power plants, agreeing to within 1% to 17% of Environmental Protection Agency (EPA) estimates for sites in the US. In a follow-up study, Nassar et al. (2021) showed that averaging multiple overpasses of the same site can improve annual emission estimates by both reducing random errors and addressing temporal variations. Reuter et al. (2019) similarly showed the value of combining OCO-2 observations of power plant plumes with NO<sub>2</sub> observations from the Sentinel-5 Precursor over six sites, comparing their estimates of cross-sectional fluxes to existing emission inventories successfully within their uncertainties. Such successful implementation of nadir and glint mode data has motivated the use of target and SAM data for similar studies: Kiel et al. (2021) utilized OCO-3 SAM and target measurements to evaluate  $X_{\text{CO}_2}$  concentrations over Los Angeles and found good agreement with coincident TCCON  $X_{\text{CO}_2}$  measurements, TROPOMI NO<sub>2</sub> estimates, and model emission estimates. In any emissions study, separating the enhancement from the background is key – Nassar et al. (2017) found that the background  $X_{\text{CO}_2}$  concentration was one of the main uncertainties in their work. Kiel et al. (2021) found that OCO-3 SAM mode measurements are able to sample both urban enhancements and background concentrations within the same overpass, so if we maintain a high fidelity of target and with OCO-3 SAM data, a single target or SAM can provide accurate information on both the enhancement and the background.

The presence of instrument and retrieval biases reduces the information content, however, especially on small spatial scales and for enhancements as small as those seen from individual point sources. OCO-2 and OCO-3 both suffer from aerosol-related biases: relying on reflected sunlight, they cannot fully distinguish between photons reflected by Earth's surface and those reflected by intermediate scatterers along the light path. The resultant changes in path length from intermediate scattering by aerosols can lead to erroneous  $X_{\text{CO}_2}$

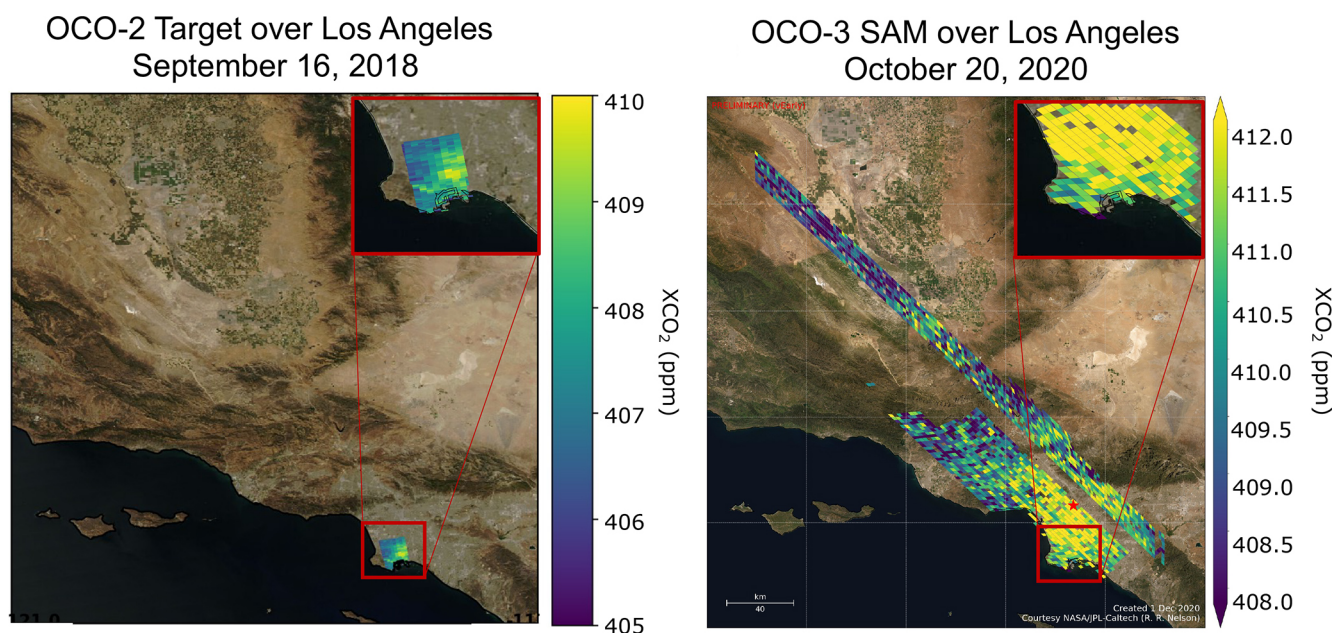


**Figure 3.** Visual comparison of target and SAM mode observations over the LA basin. The left panel and insets were generated by overlaying OCO-3 data on RGB images from NASA Worldview (Cronk et al., 2023).

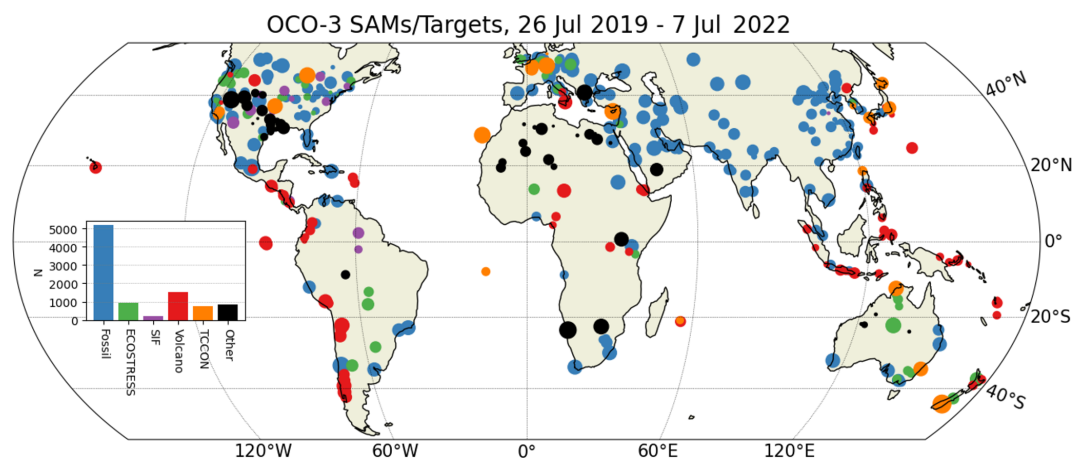


**Figure 4.** Map of all OCO-3 SAMs and targets recorded through July 2022, categorized by site type.

values (see e.g., Aben et al., 2007; Butz et al., 2009; O’Dell et al., 2012). In Target and SAM modes, especially, the misattribution of path length can be exacerbated by the quickly changing viewing geometry. In addition to aerosols, Wunch et al. (2017) and Worden et al. (2017) both evaluated OCO-2 data on regional scales to find that residual biases of up to 1.5 ppm remained compared to colocated TCCON sites and that some residual noise in OCO-2 data may be due to variations in surface properties or solar zenith angle. It was this type of small-area analysis that led to the earliest conception of a simulation-based investigation of geometry and aerosol-dependent biases, which we utilize in this study. The SB effect in vEarly, discussed in the previous section, may

be related to any of these factors: aerosol, viewing and solar geometry, or even surface properties. While we focus our study on a robust evaluation of OCO-3 SAMs, we have also observed SB in some OCO-3 targets after separating their overlapping scans. Given that the same principle of changing geometry over a constant atmospheric scene applies, we argue that the causes of SB in OCO-3 SAMs are also applicable to OCO-3 targets.

### 3 Swath bias in vEarly

In the early processing of OCO-3 SAM data, multiple SB cases were identified with each proceeding month. Initially,

case identification was done by eye, inspecting plots of the data as it was processed. The magnitude and spatial coherence of the observed  $X_{\text{CO}_2}$  biases made them the subject of curiosity and concern. The vEarly dataset includes nearly 6000 SAMs, spanning a wide variation of surface types, aerosol scenes, and solar and viewing geometries. To quantitatively identify what fraction of this collection suffers from SB, we develop an SB “flag” using the following criteria:

1. the SAM must include at least 500 soundings,
2. the SAM must include at least four swaths with at least 100 soundings apiece (SAMs typically include four to six swaths), and
3. the ratio of the standard deviation of the in-swath  $X_{\text{CO}_2}$  medians to the mean of the in-swath standard deviations is greater than 0.75.

Mathematically:

$$\begin{aligned} \text{sb\_ratio} &= \frac{\text{SD}(\text{swath } X_{\text{CO}_2} \text{ medians})}{\text{mean}(\text{swath } X_{\text{CO}_2} \text{ SD})} \\ &= \frac{\text{sd\_median}}{\text{mean\_sd}} > 0.75. \end{aligned} \quad (1)$$

In the rest of this study, we will refer to the quantity in the numerator as `sd_median` and the denominator as `mean_sd`.

Essentially, the `sb_ratio` is a form of the “coefficient of variation”, which quantifies the variability in across-swath  $X_{\text{CO}_2}$  in relation to the mean of the population variability. The `sb_ratio` requires that for cases free of SB (`sb_flag` = 0), the noise across swaths must represent less than 75 % of the noise within the scene. If the noise across swaths represents more than 75 % of the noise within the scene, we consider the scene the subject of an SB effect, and it is assigned an `sb_flag` of 1. This simple flag provides a computationally efficient means of evaluating all 5940 vEarly SAMs for the presence of SB. We acknowledge that this interpretation of `sb_ratio` assumes that any sufficient across-swath  $X_{\text{CO}_2}$  variability is due specifically to SB, meaning that real  $X_{\text{CO}_2}$  signals or other biases are negligible; this leaves room for error in our interpretation of the `sb_flag`, which we explore later in the version 10 data product in Sect. 7.

The filtering process for the OCO missions in general involves two stages: preprocessing, which eliminates soundings prior to the L2FP retrieval (also called “sounding selection”), and postprocessing, applied to the retrievals themselves. The first involves the A-band preprocessor (ABP), which is used to retrieve surface pressure and is sensitive to clouds and aerosols (Taylor et al., 2016). Retrieved surface pressures whose difference from prior estimates (`dP_abp`) are anomalously large are assumed to be contaminated by clouds or aerosols and are considered lower quality. A secondary preprocessing cloud filter is also applied, which relies on the ratio between strong and weak band-retrieved  $\text{CO}_2$  in the IMAP-DOAS preprocessor (IDP, Taylor et al., 2016).

Only sounding which passes both ABP and IDP is processed through L2FP. In postprocessing, OCO-2 and OCO-3 Lite products include a quality flag to be applied by the user, which we describe briefly in Sect. 1, with further details of vEarly quality flag construction in Osterman et al. (2020).

For our vEarly analysis, we apply a simple postprocessing quality filter to individual soundings prior to calculating the `sb_ratio`. A review of the operational quality flag in vEarly shows that an increasingly unrealistic fraction of SAMs are flagged as “bad” (quality flag of 1) due to progressive calibration errors over the vEarly record. In the sounding selection process, a `|dP_abp| < 30` filter is used to eliminate cloudy soundings before pushing “clear” soundings through to L2FP (Taylor et al., 2016). We choose in this study to use an additional postprocessing simple filter of `|dP_abp| < 16` hPa to define “good” quality soundings. A similar range of `dP_abp` is typically used in the development of the operational quality flags (Taylor et al., 2020). This alone acts as a fairly relaxed filter, but it is critical for our investigation to retain enough soundings to see the swath bias. For the rest of this study, we will refer to this as the `dP_abp` quality filter.

The collection of 5940 vEarly SAMs, spanning from August 2019 to June 2021, includes 2940 cases with 500 or more soundings ( $N > 500$ ) after the `dP_abp` filter is applied. Based on Eq. (1), 352 of those cases are flagged as having SB – about 12 %. This is a fairly significant fraction of the full dataset, not to mention that 256 of the 352 SB SAMs are urban/fossil sites, where accuracy over small areas is particularly important for fine-scale emission estimates; identification of bias and uncertainty is therefore essential. In fact, we find that SAMs over urban/fossil sites experience SB in nearly 14 % of  $N > 500$  cases, whereas only 9 % of non-fossil  $N > 500$  SAMs experience SB.

There are a number of retrieved parameters which can help diagnose correlating factors of the SB within vEarly. We provide histograms of several of these parameters in Fig. 5. The  $N > 500$  SAM collection is shown in blue, and the percentage of  $N > 500$  SAMs with SB is shown in orange. A few trends are of interest here. A larger fraction of SAMs have SB in the morning hours, with a minimum around local noon. We also see a consistently larger percentage of SB SAMs at higher solar zenith angles. These two observations combined can be interpreted as a higher frequency of SB cases when scattering effects are stronger, e.g., longer slant paths through the observed atmospheric column. A longer path length means higher aerosol optical depths, and in particular, we suspect aerosol optical depths to be of importance, based on both Fig. 5c and the historical difficulty of characterizing and accounting for aerosol effects within the ACOS algorithm (Worden et al., 2017; Wunch et al., 2017; Nelson and O’Dell, 2019). This hypothesis aligns with the fact that so many of our SB cases are at urban/fossil sites, which tend to be polluted.

Trends in the mean retrieved albedo also show higher fractions of SAMs at higher albedos, particularly in the  $\text{O}_2$  A-

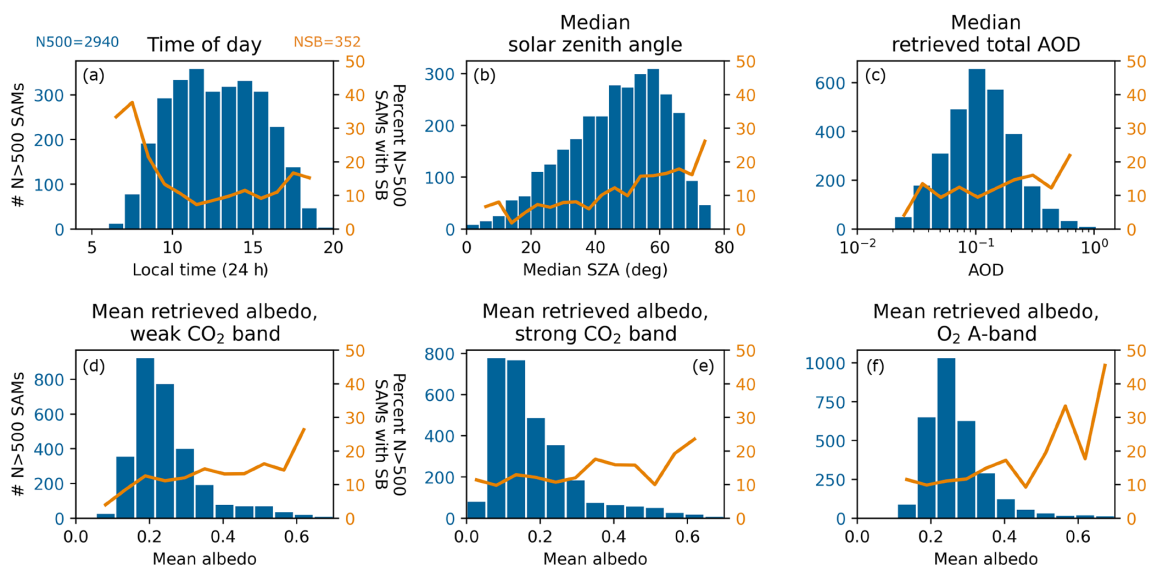


**Figure 5.** Histograms showing the distribution of various retrieval parameters across 2940 vEarly SAMs with 500 soundings or more. The orange line indicates the percentage of SAMs in each bin which have been flagged as having SB. This percentage was only calculated for bins containing at least 10 SAMs.

band. This analysis confirms our early subjective observations, which pointed us toward scenes with brighter surfaces and higher AODs.

#### 4 Simulation setup

Motivated by the results in the previous section, we turn to realistic simulations to systematically evaluate the sensitivity of algorithm-induced swath bias to parameters such as AOD and surface albedo. We begin with the actual instrument time and geometry information, determine realistic atmospheric profiles based on various model inputs, and finally calculate the top-of-atmosphere radiance spectra. These simulations are variants of the simulation system described in O’Brien et al. (2009).

##### 4.1 Generating atmospheres

The first step in the simulation process is to create a simulated atmosphere. We use the real OCO-3 geometry data from the SAM of interest to obtain location information such as date and time, latitude and longitude, and ISS, PMA, instrument, and solar geometry.

NOAA’s CarbonTracker version 2019B (CT2019B) is used for atmospheric carbon data (Jacobson et al., 2020). Native CT2019B CO<sub>2</sub> mole fractions are provided globally at 3-hourly, 3° longitude by 2° latitude resolution, with 35 vertical layers. Data are available through the end of 2018; in this study, we simulate three SAMs taken in 2020, using CT2019B data from the relevant day in 2018. Any mean offset in our simulated X<sub>CO<sub>2</sub></sub> values compared to the observed OCO-3 data can thus be attributed to the annual growth rate

since 2018 – around 2.4 ppm yr<sup>−1</sup> (Tans and Keeling, 2022). We have not accounted for this offset in our simulations, as our investigation hinges on changes in small-scale spatial patterns rather than global mean increases.

We use NOAA’s National Centers for Environmental Prediction (NCEP) reanalysis for meteorological data. NCEP near-real-time data are available at 6-hourly global coverage on a 2.5 × 2.5° grid and 17 pressure levels (NCEP/NCAR Reanalysis 1; Kalnay et al., 1996; NOAA/NCEP, 2022). We apply a hypsometric surface pressure adjustment, and we use the specified month and day from 2018, as with CarbonTracker. The resampled CT2019B and NCEP reanalysis data are then combined with MODIS surface reflectances to build our final meteorology and scene datasets. The MCD43A1 MODIS BRDF/Albedo product used here is available globally at 500 m resolution daily (Schaaf and Wang, 2015).

Our next step is to build a simple yet semi-realistic aerosol and surface scene. For a given SAM, we only include one aerosol type at a time and always exclude water and ice clouds. We keep the specified vertical aerosol profile uniform across the scene. Simulated aerosol types are prescribed in the L1b simulator framework. A full list of the aerosol types available in the simulator can be found in O’Brien et al. (2009), but in this study, we only utilize two: a coarse “dust” type and a fine “clean continental” type. Aerosol effective radius, single scattering albedo, and other optical properties are derived from Dubovik et al. (2002). These aerosol types are different than those used in the ACOS L2FP retrieval (discussed in Sect. 5). To construct our profiles, we begin with an existing aerosol profile from a resampled Cloud-Aerosol Lidar with Orthogonal Polarization (CALIOP) 05kmALay monthly field (Winker et al., 2007). The parameters for the

selection of this initial profile are loose, because once it is chosen, we can change the aerosol type, adjust the layer up or down to any native CALIOP vertical pressure level, and then scale the number densities to achieve our specified optical depth. Previous studies have shown radiances to be relatively insensitive to the geometric thickness of the aerosol layer (Butz et al., 2009; Frankenberg et al., 2012), so we do not control for this; it is determined by only the pressure layer thickness at the specified height. The mechanism used to adjust the vertical height of the aerosol layer puts the top of the layer at the native CALIOP pressure level closest to specified pressure: for example, if a pressure of 800 hPa is input, the top of the aerosol layer may actually sit at 793 hPa. The exact value varies slightly based on the date and surface pressure, so for simplicity, we will refer to the approximate input heights, e.g., 750, 800, or 900 hPa. We apply our single profile, along with its associated surface elevation and surface reflectivity, to every sounding in the SAM.

## 4.2 Generating L1b radiances

Simulated radiances are generated by a forward model that has been used previously for simulation studies of GOSAT, OCO-2, and OCO-3, such as in Eldering et al. (2019). The radiative transfer module uses the specified aerosol, physical, and surface properties as inputs, along with geometry information. In this study, we calculate the gas absorption optical depths using the absorption coefficient (ABSCO) lookup table v5.1 (Payne et al., 2020). Options for surface treatment include a specified Lambertian albedo, a MODIS-derived Lambertian albedo, and a MODIS-derived BRDF albedo. We use the first when testing specific surface albedos in the three bands, and we use the last when testing aerosol properties with realistic albedos. We do not account for changes in surface topography, i.e., a fixed elevation is used for all soundings within a scene. Rayleigh scattering is calculated, as well as the solar spectrum, derived from a solar model described in Bösch et al. (2006). The solar spectrum is Doppler shifted to account for the reference frame of the instrument; then, we obtain a “measured” spectrum via an instrument model, which convolves the instrument line shape (ILS) function with the simulated Doppler-shifted spectrum. We do not add instrument noise in this work for clarity, but doing so would add a component of random error to the radiances and hence to the retrieved  $X_{\text{CO}_2}$  (Connor et al., 2016).

## 5 ACOS L2FP retrieval algorithm

The ACOS algorithm is well documented (O’Dell et al., 2012, 2018); here we provide a brief summary. For the simulated data, as with operational OCO data, predominant cloud screening is performed by the O<sub>2</sub> A-band preprocessor (ABP), documented in Taylor et al. (2016). The A-band provides a means of accurate surface pressure retrieval and uses

the difference between retrieved and prior surface pressure (dP) to determine the presence of clouds.

After filtering by the ABP, the selected soundings are run through the L2FP retrieval. The retrieval utilizes an optimal estimation approach, iteratively minimizing a cost function to produce the most likely observed radiances, and ultimately, an estimate of  $X_{\text{CO}_2}$ . The L2FP state vector also includes a posterior CO<sub>2</sub> profile, aerosol optical depths, surface albedos, and surface pressure, among several other variables. Spectra generated by the retrieval utilize a radiative transfer model similar to the L1b simulator, which is described in the previous section. A full description of the ACOS retrieval algorithm is available in O’Dell et al. (2012). The OCO-3 vEarly dataset was produced using version 10 of the ACOS algorithm.

The L2FP algorithm used in our simulation study is v8 (O’Dell et al., 2018) but with the use of the newer ABSCO v5.1.0 (Payne et al., 2020) in order to match the simulator spectroscopy. Recall that ACOS v9 did not include any changes to the L2FP retrieval itself and was a reprocessing of the L2 Lite files only, mainly to account for corrections in the OCO-2 pointing (Kiel et al., 2019). At the start of this work, the ACOS v10 L2FP was still in development. The retrieval state vector includes five aerosol types (O’Dell et al., 2018): always retrieved are water cloud, ice cloud, and a stratospheric aerosol; the remaining two aerosols are fixed types from the Modern-Era Retrospective Analysis for Research and Applications 2 (MERRA2, Gelaro et al., 2017) and vary based on the time and location of the SAM. Prior meteorology comes from GEOS-5 FP-IT (Rienecker et al., 2008) and is used for temperature profiles, water vapor profiles, and surface pressure.

## 6 Simulation experiments

Here we discuss the case selection and results of our simulated SB experiments. In this introduction, we test two SB SAMs from vEarly to see whether we can recreate the observational SB using simulated data. We then focus on three SAMs over a single representative target location and use their geometry as templates to test the SB in a more complete scene state space: we manipulate each SAM to include various aerosol types, heights, and optical depths with a constant surface elevation and reflectivity. Finally, we hold aerosols constant while testing changes to surface albedo in all three bands.

To begin our investigation we choose two desert scenes where the vEarly operational retrieval indicates an SB. The first, over Australia, is a target for comparison with Ecosystem Spaceborne Thermal Radiometer Experiment on Space Station (ECOSTRESS, also on board the ISS) observations; the second is an urban site near Tabriz, Iran. Maps of several vEarly retrieved parameters for both SAMs are shown in Figs. 6 and 7, with no filtering, in order to maximize

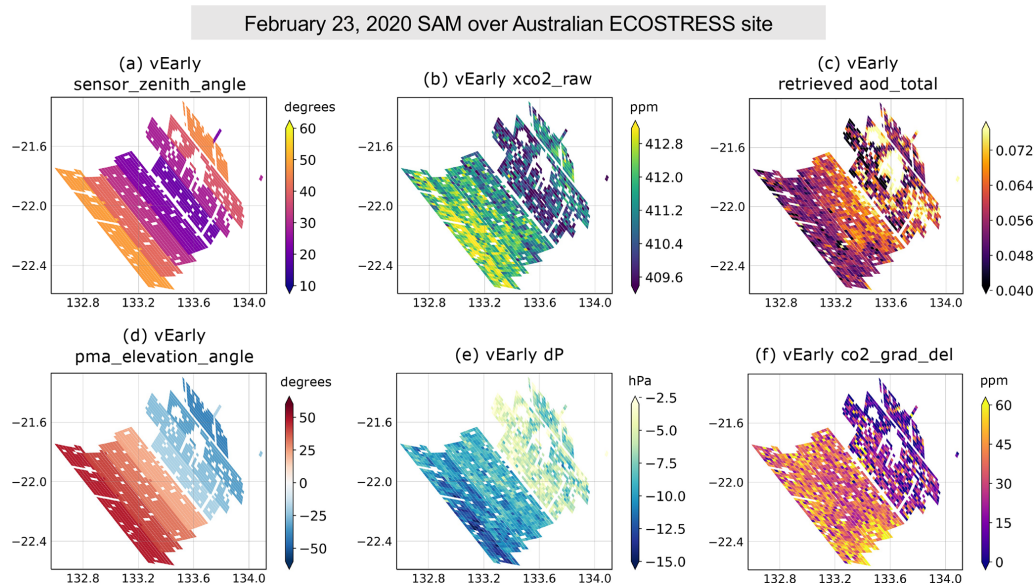


**Figure 6.** Maps of several retrieved and geometry-related parameters for a vEarly SAM over an Australian ECOSTRESS site on 23 February 2020.

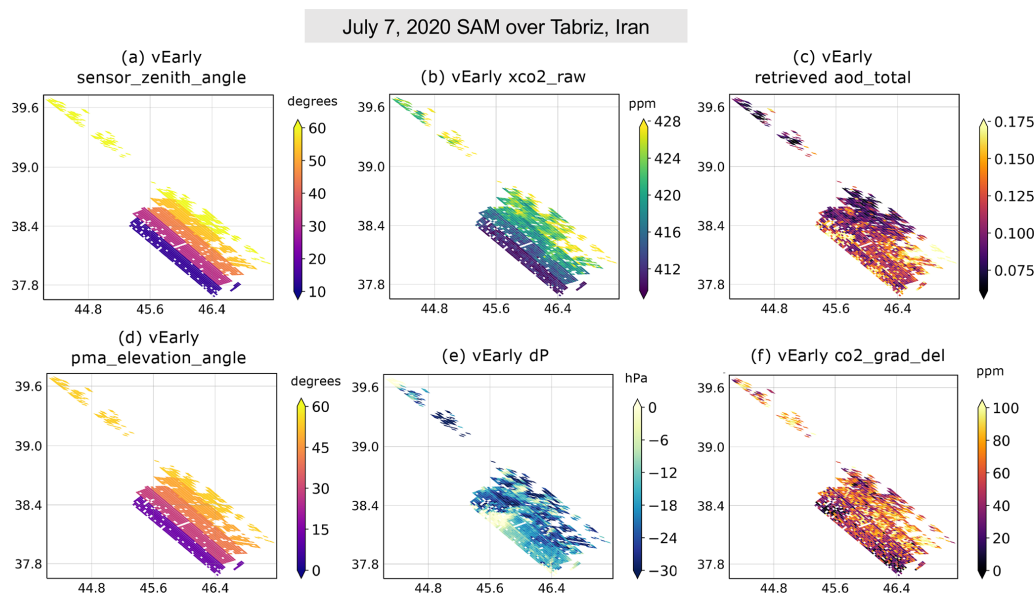


**Figure 7.** Maps of several retrieved and geometry-related parameters for a vEarly SAM over Tabriz, Iran, on 7 July 2020.

comparison to simulations. In both figures, SB patterns in  $X_{CO_2}$  – panel (b) – are primarily correlated to changes in the viewing geometry, which we represent in the two left panels. Panel (a) shows the sensor zenith angle, and panel (b) shows the PMA elevation angle, a measurement of the geometry of the pointing mechanism, where positive angles indicate forward-looking observations, and negative angles indicate backward-looking observations.

In panels (c), (e), and (f), we show a few other retrieved parameters which the retrieval might adjust when attempting to

characterize geometry-driven aerosol effects. Panel (c) shows the total retrieved AOD (labeled aod\_total), and panel (f) shows co2\_grad\_del, the difference between retrieved and prior  $CO_2$  concentration in the upper and lower portions of the retrieved column (the exact calculation can be found in Osterman et al., 2020). The SAM over Iran in Fig. 7 may show a hint of SB in these two parameters, but they appear quite smooth in Fig. 6. This may be related to higher AODs over the Iran SAM (maximum AOD near 0.35 versus maximum near 0.25 in the Australian SAM, per MODIS esti-

mates) driving stronger geometry-related aerosol scattering effects. Real AOD variations or interactions with heterogeneous surface albedo may dominate the visible signal, rather than geometry effects. In panel (d) of these figures, we show dP values, which appear to reflect some SB in Fig. 6 but in Fig. 7 are dominated by local topography patterns. In these three retrieved parameters – aod\_total, dP, and co2\_grad\_del – we expect that in simulations where geometry is the primary variable, its effects will be visible.

Our first simulations are thus a simple test of this hypothesis. For each date, we apply a constant aerosol profile and type across each scene, set a constant surface elevation and reflectivity, and choose realistic AODs based on local Multi-Angle Implementation of Atmospheric Correction (MAIAC) data, which use MODIS data to derive improved aerosol estimates (Lyapustin et al., 2011; MODIS Land Science Team, 2019, MAIAC data accessed via NASA Worldview). Figures 8 and 9 show the results of these initial simulations – note that the color bar ranges are different than in Figs. 6 and 7.

We find that simulated spectra derived from simple aerosol scenes are successfully able to generate SB patterns qualitatively similar to those in the operational vEarly data. The general orientation of the observed SB is replicated in both simulated SAMs, but the magnitude of the SB tends to be smaller relative to the observed data. In the absence of more complex aerosol and surface scenes, we do see geometry-driven swath bias in aod\_total, co2\_grad\_del, and dP, although the range of values can be quite different than in the observations – for example, the range of aod\_total in Fig. 9 is much larger than in Fig. 7. This may indicate that the aerosol profile constructed for the simulation does not match that observed by the satellite.

We proceed with a series of simulations to evaluate this possibility, testing SB response to various aerosol and surface scenes. Note that because we do not add noise to our simulations, and eliminate many other sources of variability, the denominator of Eq. (1) will be small in simulated data compared to the observed data, so the sb\_ratio will typically be much larger. We set the sb\_ratio = 0.75 threshold for the SB flag using observed data, but it would be larger for simulations – in order to avoid using two different scales of sb\_ratio, we will simply use sd\_median as a measure of relative SB strength when discussing simulations. We use the terms sd\_median and SB strength interchangeably to describe the same simulated quantity.

### 6.1 Case selections for controlled testing

From the initial simulation tests over Australia and Iran, we single out the Australian non-fossil site as a target for further simulation work. This is a desert site and should lack influence from local fossil fuel emissions due to its remote location. OCO-3 has taken several SAMs over this site at the time of analysis, at varying times of day and with vary-

**Table 1.** Key metadata and statistics for three Australian ECOSTRESS site SAMs chosen for simulation work.

Date	23 February 2020	4 April 2020	8 May 2020
Orbit no.	4573	5204	5731
No. soundings	2104 (2077)	2465 (2461)	2337 (2337)
Local time	16:09	10:10	11:08
Min/max SZA	55.3/57.0°	45.6/47.4°	44.2/44.9°
MAIAC AOD	0.15	0.08	0.12
sb_flag	1 (1)	0 (1)	0 (0)
sb_ratio	0.98 (1.05)	0.55 (0.76)	0.28 (0.28)
sd_median	0.86 (0.76)	0.37 (0.39)	0.25 (0.21)
mean_sd	0.88 (0.73)	0.68 (0.51)	0.88 (0.75)

sb\_flag, sb\_ratio, sd\_median, and mean\_sd are all defined as in Eq. (1). These are calculated for raw vEarly soundings with no filtering applied. Values in parentheses are calculated after vEarly bias correction and dP\_abp filtering are applied. MAIAC AOD is a rough estimate derived from data available on NASA Worldview.

ing SB signals present according to our criteria. We choose three, which are pictured in Fig. 10. Metadata and key statistics are provided in Table 1. By examining three SAMs from the same site, we are able to investigate the differences in atmospheric state and/or observation geometries that drive the operational SB, in addition to using their different geometries as templates for a broader array of synthetic scenes, as mentioned previously.

The strongest example of SB is present on 23 February 2020, which served as our first SAM SB test in the previous section. The sb\_ratio (see Eq. 1) in this SAM is 0.98 – well over our required threshold of 0.75 for the sb\_flag. We also examine a “borderline” SB case from 4 April 2020, where the raw data have a sb\_ratio of 0.55, but after bias correction our sb\_flag is triggered by a sb\_ratio of 0.76, and some small across-swath gradient of approximately 1 ppm magnitude appears to be present (Fig. 10b). The third SAM is from 8 May 2020 and has a very low sb\_ratio of 0.28 (Fig. 10c). The MAIAC AODs listed in Table 1 will be used in simulations unless otherwise stated. Figure 11 provides context for the observation and solar geometries for each of these dates. We include scattering angle, which is the angle between incoming solar photons and outgoing photons which reach the OCO-3 sensor. Pure forward scattering occurs at 0° and pure backscattering occurs at 180°. The 4 April case has the largest range of scattering angles, approaching 170° in the final two swaths. The 23 February date has the highest solar zenith angle, at 16:09 local time, and has the smallest scattering angles.

Figure 12 shows the reference aerosol profiles used on each of these three dates. AODs used in this figure match those listed in Table 1, and the tops of the aerosol layers have been adjusted to a height near 800 hPa. In our simulation tests, we will test sensitivity to aerosols by changing the aerosol types (Sect. 6.2), shifting these layers to different vertical levels (Sect. 6.3), and scaling the number densities to

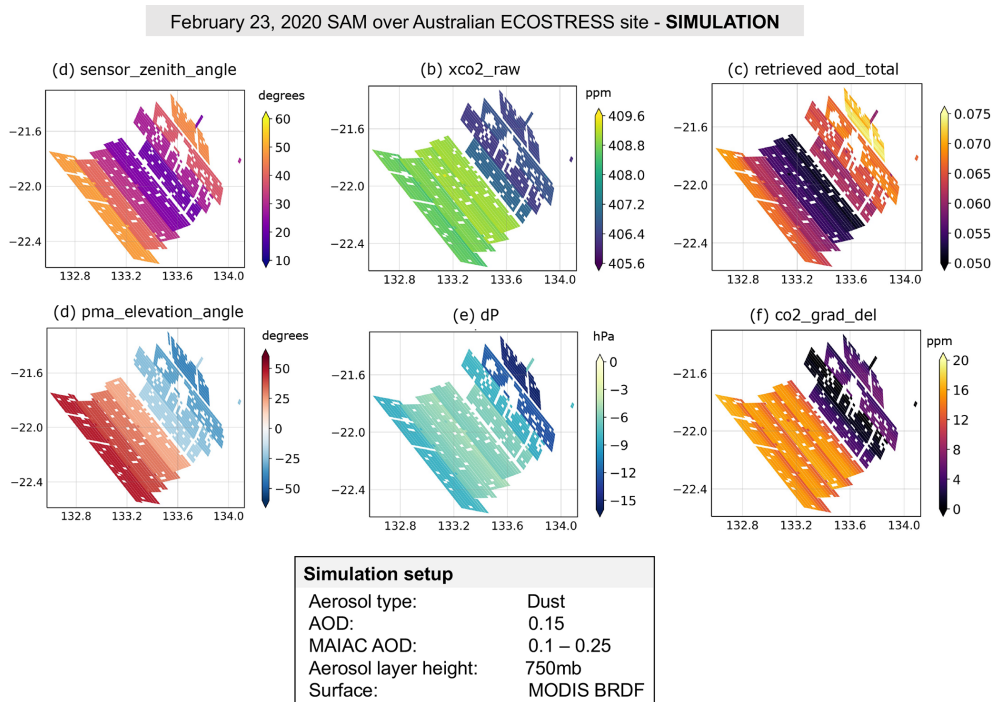


Figure 8. Maps of several retrieved parameters from our first simulation of the 23 February 2020 SAM over Australia.

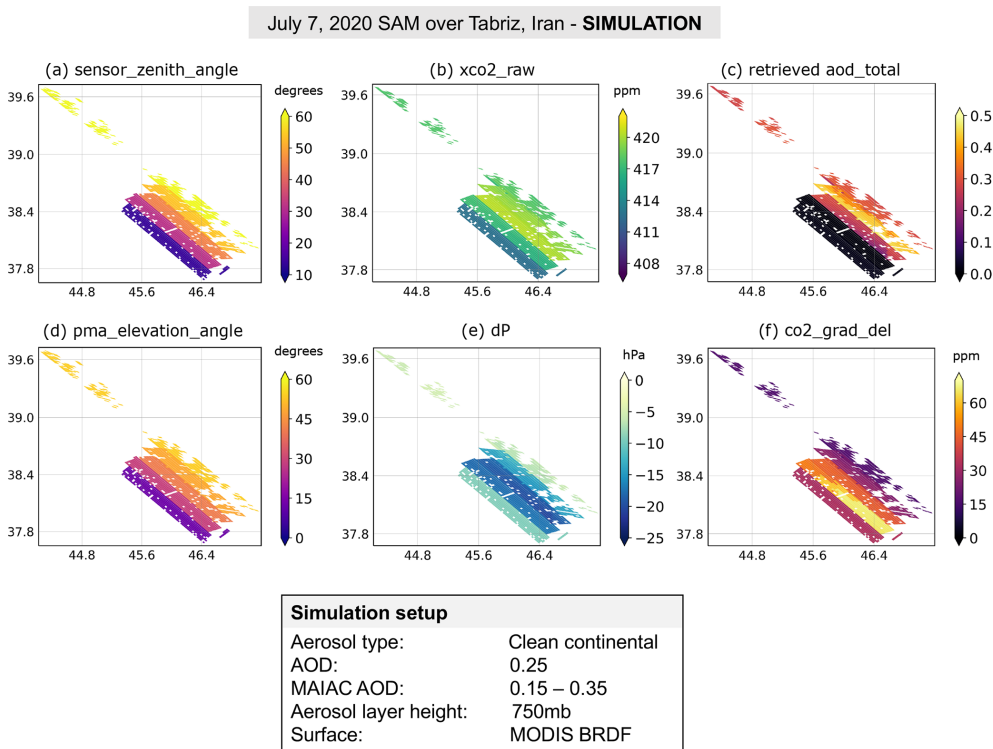
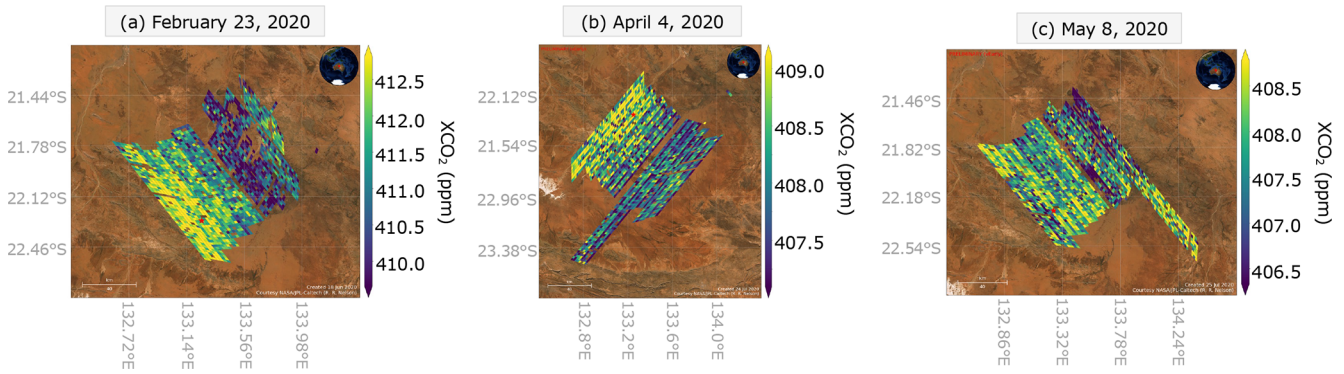
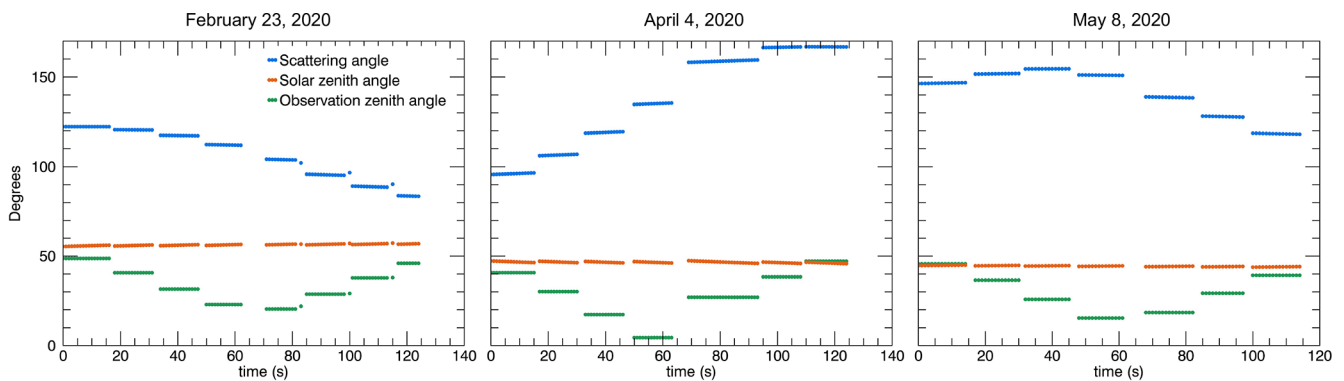


Figure 9. Maps of several retrieved parameters from our first simulation of the 7 July 2020 SAM over Tabriz, Iran.



**Figure 10.** Three OCO-3 vEarly SAMs, shown with no filtering or bias correction, all over the same ecostress\_au\_asm observation site. These three SAMs were chosen for simulation tests due to their varying degrees of apparent SB, as well as different observation and solar geometries.



**Figure 11.** Geometry data for the three simulated Australian desert SAMs.

adjust the AOD (Sect. 6.4). We will further test sensitivity to surface albedo (Sect. 6.5).

### 6.2 Aerosol type testing

For each of the three SAMs, we test two different aerosol types: one coarse mode, a dust type, and one fine mode, a clean continental type, both of which are realistic given the remote desert setting. The aerosol layers are at a height near 800 hPa, and each date uses the same optical depth (listed in Table 1) for both aerosol types, so only the number densities change.

The results of these tests are shown in Fig. 13 and listed in Table 2. We find in the February case that the clean continental aerosol type produces a much stronger SB than the dust mode, with  $sd\_medians$  of 1.16 and 0.23 ppm, respectively. The 8 May SAM shows a similar result, with stronger SB using the clean continental type aerosol, although the increase in SB is much smaller. The February and May cases have similar AODs – 0.15 and 0.12 – so the smaller SB response on 8 May may be attributed to its smaller mean and range of SZA.

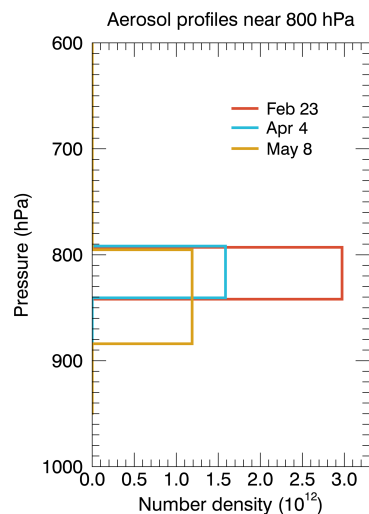


**Figure 12.** Profiles illustrating aerosol layer shape used for the three simulated SAMs. This example shows dust layers whose tops are placed at the native CALIOP pressure level closest to 800 hPa.

The response is opposite for the 4 April case: the dust type aerosol produces a stronger SB. This may be related

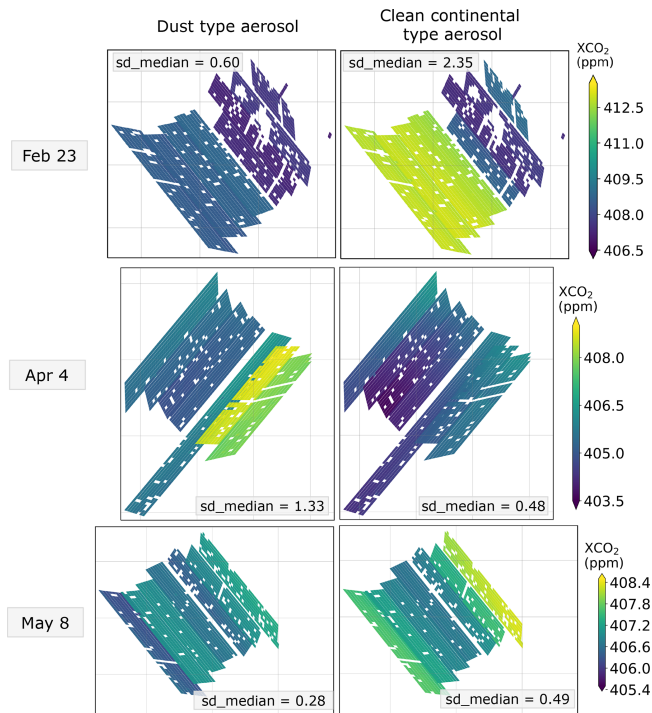


**Figure 13.** Simulated  $X_{CO_2}$  using two different aerosol types for all three SAM dates over the Australian ECOSTRESS site.

**Table 2.**  $sd\_medians$  (ppm; from Eq. 1) for simulated  $X_{CO_2}$  in the ECOSTRESS AU SAM site using different aerosol types.

Date	Dust type aerosol	Clean continental type aerosol	Operational
23 February	0.60	2.35	0.86
4 April	1.33	0.48	0.37
8 May	0.28	0.49	0.25

Simulations included in this table use realistic AODs for each date based on MAIAC estimates and an aerosol layer lofted to near 800 hPa.

to the high scattering angle in the final two swaths – nearly  $170^\circ$ , per Fig. 11. However, an investigation into the scattering phase functions for these two aerosol types revealed no correlation relative to the SB strength, for any of the three dates.

However, in terms of SB orientation, the 8 May case illustrates particularly well the fact that different aerosols produce different geometry-dependent responses: the location of the highest and lowest  $X_{CO_2}$  values occurs in different swaths depending on the aerosol type. This makes sense given the unique optical properties of each aerosol type but would require further study to predict with quantitative skill. We conclude that the physics of SB, in terms of both magnitude and direction, are highly dependent on the aerosol type and are complex enough to warrant further study.

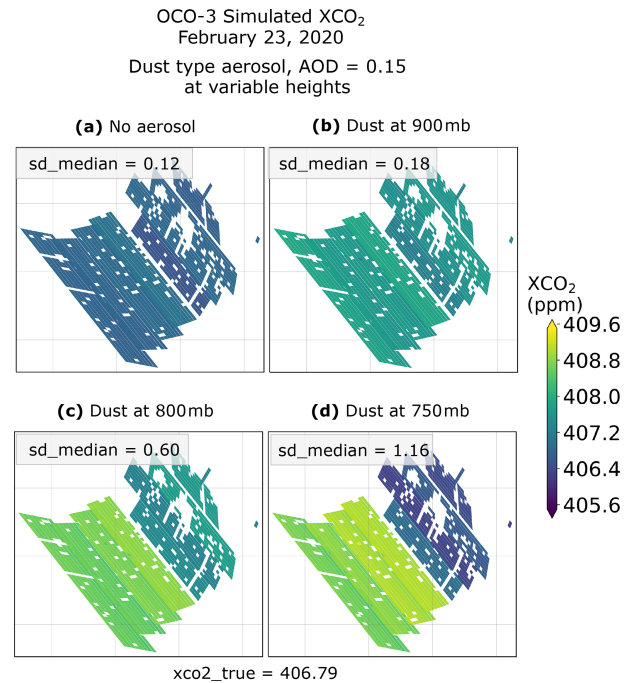


**Figure 14.** Simulated  $X_{CO_2}$  using a dust type aerosol at three different heights, with an AOD of 0.15, over the Australian ECOSTRESS SAM site on 23 February 2020.

### 6.3 Aerosol height testing

Using dust type aerosols, we test a simple profile at three heights for each SAM. We take the base profile for each date, as shown in Fig. 12, and simply loft the aerosol layer to the desired pressure level: either 900 hPa (near surface), 800 hPa (mid-level), or 750 hPa (higher level). These are chosen arbitrarily to represent a typical range of tropospheric aerosol heights, spanning roughly a few vertical kilometers.

We also include a clear-sky, no-aerosol run as a baseline for retrieval behavior. Figure 14 shows the results of this experiment using a dust type aerosol with an AOD of 0.15 in the 23 February 2020 case. Table 3 shows that there is a positive correlation between aerosol height and  $sd\_median$  – i.e., as the aerosol layer is lofted, the strength of the SB increases.

As indicated by Table 3, the 4 April and 8 May cases respond similarly to changes in aerosol layer height. The SB is always stronger in simulations with aerosol than in simulations without; it increases in strength as we move the aerosol layers higher in the column. The relative increase between the 900 and 750 hPa aerosol layer varies between cases – the 4 April case has the strongest change in SB, which again could be related to its broad range of scattering angles and high scattering angles near the end of the scan. The range of  $sd\_medians$  on 8 May is notably smaller than that of either 23 February or 4 April, similar to its response to different aerosol types. This could again be due to 8 May having the

**Table 3.** sd\_medians (ppm) for simulated  $X_{\text{CO}_2}$  in the ECOSTRESS AU SAM site using different aerosol heights.

Date	No. aerosol	Aerosol near 900 hPa	Aerosol near 800 hPa	Aerosol near 750 hPa	Operational
23 February	0.12	0.18	0.60	1.16	0.86
4 April	0.22	0.47	1.33	1.81	0.37
8 May	0.18	0.21	0.28	0.39	0.25

Simulations included in this table use realistic AODs for each date based on MAIAC estimates. All use a dust type aerosol.

**Table 4.** sd\_medians (ppm) for three different AODs in each simulated SAM.

Date	AOD = 0.0	AOD = 0.10	AOD = 0.20	AOD = 0.35
23 February	0.12	0.43	0.74	0.97
4 April	0.22	1.67	2.94	3.60
8 May	0.18	0.27	0.41	0.70

Simulations included in this table use realistic AODs for each date based on MAIAC estimates. All use a dust type aerosol.

lowest range of SZAs relative to the other two dates, per Table 1 and Fig. 11.

The correlation between SB strength and aerosol layer height is consistent for both large and small aerosol types, as revealed by additional testing using the clean continental aerosol type. Operationally, this makes SB more likely to be detectable beyond scene-typical noise, both by eye and by our SB flag, if there is aerosol higher in the atmospheric column. In addition to differences in viewing geometry, this could be one reason that SB appears in some cases and not others in real measurements.

#### 6.4 Aerosol optical depth testing

In this section we test three aerosol optical depths for each SAM: one low (0.1), one moderate (0.2), and one high (0.35). These are chosen to represent a realistic range typically seen over the Australian ECOSTRESS site according to MAIAC. We use a single layer of dust aerosol at a height near 800 hPa. Results are shown in Fig. 15. Per Table 4, we find that SB strength increases with increasing AOD in all three Australian SAMs, with 4 April as the exceptionally strong SB case once again – the  $X_{\text{CO}_2}$  values change much more significantly in the final two swaths with high scattering angles than in the others. As in the aerosol height tests, the SB is always stronger in the presence of aerosols than in the AOD = 0.0 test case. We are therefore more likely to see SB over high-AOD scenes.

#### 6.5 Surface albedo testing

Per discussion in Sect. 3, a larger fraction of scenes with high retrieved surface albedo, in any of the three spectral bands, is flagged as having SB. In this section, we assign a range of

surface albedos to our simulated SAMs to strategically test the SB response.

We test surface albedos ranging from 0.1 to 0.6 in each of the three bands, which covers a realistic range of albedos over land. When varying one band, we hold albedo constant in the other two bands at a realistic value for this site: O<sub>2</sub> A-band (O2A) at 0.25, strong CO<sub>2</sub> (SCO2) band at 0.25, and weak CO<sub>2</sub> (WCO2) band at 0.30. The functionality of the simulator requires that when prescribing a specific surface albedo, we model the scene using a Lambertian surface. (This is different from the previous sections, where the simulator always utilizes a BRDF surface.) The ACOS retrieval, however, uses a BRDF surface model.

These simulations use the same vertical aerosol distributions as shown in the previous sections; the AOD on each date is the realistic MAIAC value listed in Table 1, and each layer is near 800 hPa. All three dates use the dust aerosol type.

The top row of Fig. 16 shows the results of the albedo tests for all three simulated SAM dates, with no filtering applied to the simulated retrievals. On each date, we compare the same number of soundings across all six albedos. The SB is highest at lower albedos, particularly for the February and April SAMs; this is the opposite trend we expect based on our analysis in Sect. 3. However, over low O2A albedos, our dP\_abp filter removes some soundings that contribute to swath bias, as shown in the bottom row of Fig. 16. The dP\_abp filter does not, however, remove any soundings when the WCO2 and SCO2 albedos are low. This makes some sense, as the O<sub>2</sub> A-band is most skilled at seeing aerosols and would best pick up on them with a high contrast between a dark, low-reflective surface and a bright, high-reflective aerosol.

From this exercise, we surmise that the trend toward SB at higher albedos observed in Sect. 3, Fig. 5, is not because SB is more likely to occur over bright scenes. In fact, stronger SB tends to occur at lower albedos. The retrieval, however, is more skilled at differentiating aerosols over dark surfaces, whereas it has trouble identifying aerosols over bright surfaces. This makes our quality filtering more effective at removing aerosol-related effects – including those of SB – over dark surfaces so that SB is more likely to slip past our filters when the surface is bright. This conclusion reinforces the fact that the presence of SB is intimately linked to the presence, and our retrieval's treatment, of aerosols.

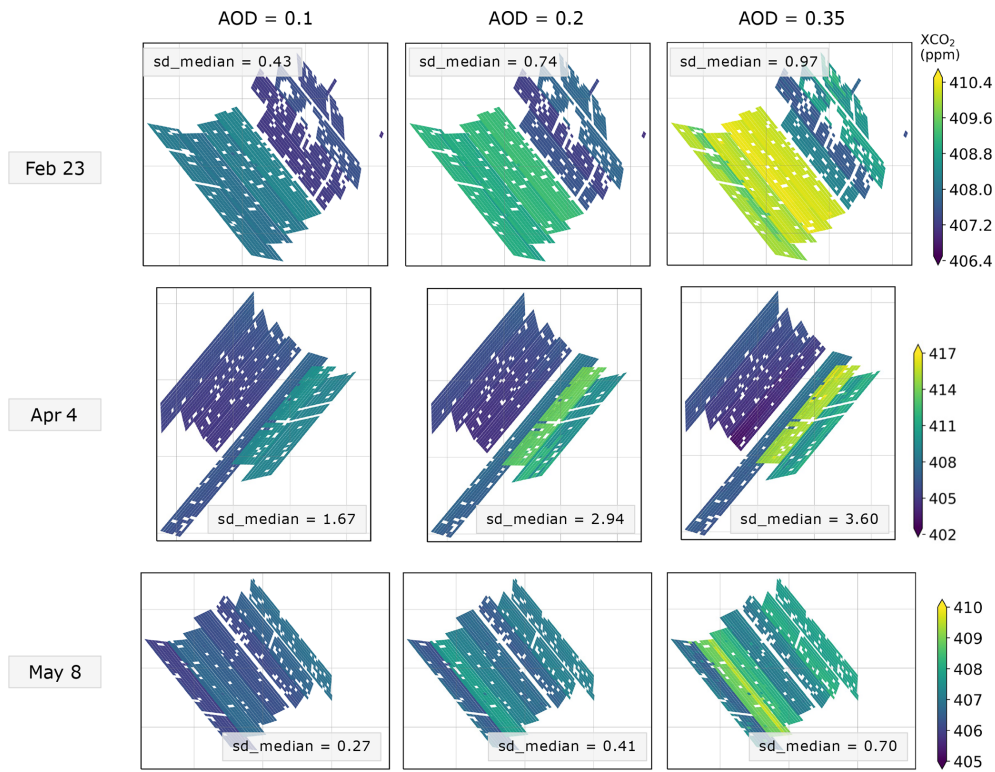


**Figure 15.** Retrieved  $X_{CO_2}$  using a simulated dust type aerosol near 800 hPa and two different optical depths for all three simulated SAMs.

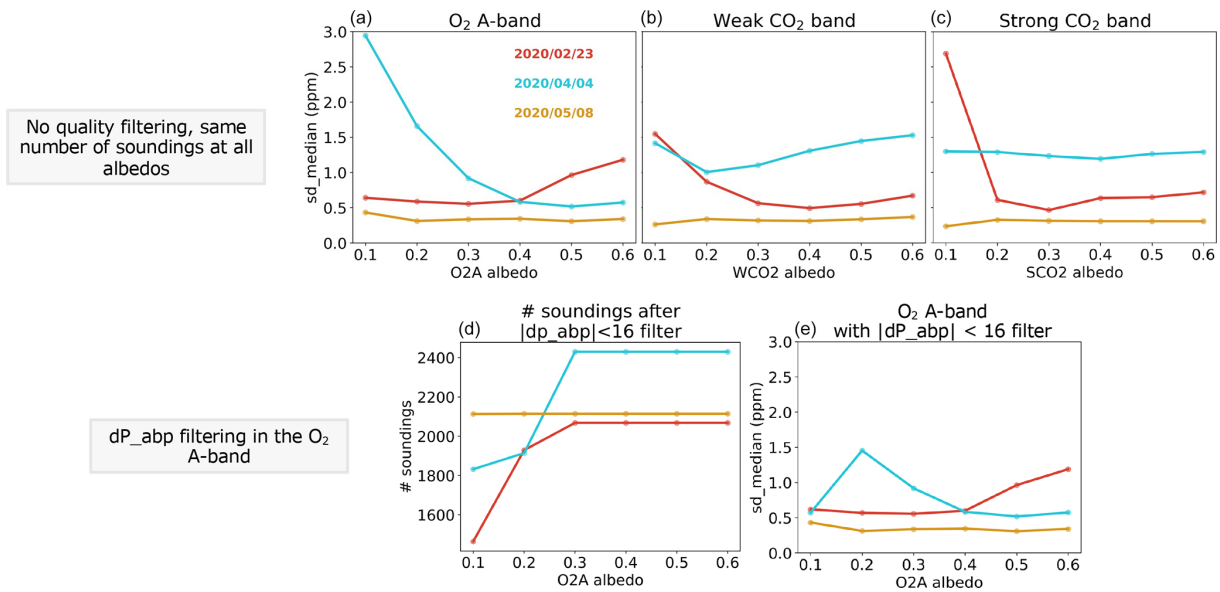


**Figure 16.** SB strength ( $sd\_median$ ) depending on surface albedo in each of the three OCO-3 bands. Panels (a)–(c) include no quality filtering, and the number of soundings per day is the same for each albedo run. Panels (d) and (e) show how  $dP\_abp$  filtering affects  $sd\_medians$  in the  $O_2$  A-band (it has no effect in the other two bands).

## 6.6 Simulation summary

In our simulation work, we show that the large changes in  $X_{\text{CO}_2}$  between swaths are primarily correlated to the changing viewing geometry and that by eliminating other sources of variability within a SAM, we can simulate the purely geometry-driven response within the retrieval. We choose three SAMs over the same Australian desert site which represent a range of SB signals, solar zenith angles, and scattering angles. For each SAM, we test an aerosol-free scene and four parameters: aerosol type, aerosol height, aerosol optical depth, and surface albedo. Aerosol-free scenes suffer from little to no SB, but we find that SB increases with both aerosol height and optical depth and that the aerosol type changes the SB strength in different ways depending on some complex interplay of aerosol optical properties and geometry. Lower surface albedos tend to induce a stronger SB, again depending on the observation and viewing geometry – but quality filtering using the  $\text{O}_2$  A-band is skilled at identifying aerosols over dark surfaces and effectively removes erroneous measurements, leaving more SB at higher albedos where it is harder to distinguish aerosols from the bright surface beneath.

Figure 17 shows  $\text{sd\_median}$  versus each of our independent parameters on the same scale. We attempt to represent some realistic range of values of each parameter, in order to be able to compare their effects. All four parameters have the potential to induce quite a large SB in our simulated SAMs, with high AODs inducing the highest  $\text{sd\_medians}$  of more than 3 ppm. We only tested AODs as high as 0.35, although higher AODs are sometimes observed – but typically, those are eliminated by quality filtering. Low  $\text{O}_2\text{A}$  albedos produced the second strongest SB in our simulations but similarly are often mitigated by our  $\text{dP\_abp}$  filter. We acknowledge that none of the  $\text{sd\_medians}$  shown here are as high as are sometimes observed in other SAMs – occasionally exceeding 10 ppm, such as in the Tabriz example shown in Fig. 7 – but we hypothesize that testing an even broader range of aerosol types, optical depths, or observation angles would produce such results. Biases or real variations in  $X_{\text{CO}_2}$  derived from additional complexity in real scenes can also enhance this signal – varying surface albedo or topography, for instance.

These simulation studies reveal that SB is primarily and intimately connected to the presence of aerosols and the interplay of their optical properties with the solar and instrument viewing geometries. We now have a better understanding of the types of scenes that are likely to suffer from SB – those with high aerosol depths, or aerosols that are lofted higher in the atmospheric column, and in geometries with broader ranges of observation and solar zenith angles. Future work may involve a more detailed study of how the physics of aerosol optical properties with viewing and solar geometries combine to produce an SB response.

## 7 Swath bias in OCO-3 version 10

Our analysis thus far has focused on vEarly, but the recent OCO-3 version 10 (v10) dataset includes a number of updates which has the potential to mitigate SB effects. This section provides a brief summary of those changes, and explores their effect on SB in the v10 SAM collection.

Key v10 updates relevant to our study can be summarized as follows:

- A geolocation error of up to 20 km in vEarly was reduced, with more current values ranging from a few hundred meters to about 2 km.
- Improved calibration algorithms account for lamp aging.
- A longer empirical orthogonal function (EOF) training dataset for v10 captures changes in spectral shape due to ice buildup on focal plane arrays.
- Sounding selection criteria for v10 L2FP processing were updated to include the IDP  $\text{CO}_2$  and  $\text{H}_2\text{O}$  ratios, which significantly reduces the number of soundings processed in certain v10 SAMs relative to vEarly.
- Operational L2FP postprocessing quality flags in vEarly eliminated a progressively larger fraction of “good” soundings. In order to see SB effects, we instead use a  $\text{dP\_abp}$  filter in this work. Updated quality flags in version 10 retain a lower, more realistic number of soundings per SAM compared to vEarly operational flags and eliminate a larger number of soundings relative to our  $\text{dP\_abp}$  filter. This change is highly coupled with the EOF improvements described in the previous bullet.
- A parametric  $X_{\text{CO}_2}$  bias correction term was added in v10, accounting for biases related to the retrieved weak  $\text{CO}_2$  band albedo, derived from a training dataset which covers a longer time period than that of vEarly.
- Based on the larger training dataset, all coefficients in the parametric bias correction were updated. This includes the  $\text{dP}$  bias correction term coefficient, which was increased from smaller than  $-0.1$  to  $-0.62$ . The new value is more in line with expectations, based on experience with OCO-2.

Operational v10 quality filtering is much more thorough than our simple  $\text{dP\_abp}$  attempt, and as far as bias correction, from our work with vEarly, we expect that the stronger  $\text{dP}$  bias correction term in particular may have a significant effect on SAMs’ SB. In particular, our February SAM exhibited some correlation between  $X_{\text{CO}_2}$  and  $\text{dP}$ , and we see a similar pattern in a number of other vEarly SAMs. For mitigation of SB, simple linear bias correction derived solely from  $\text{dP}$  proves more effective in those cases than the

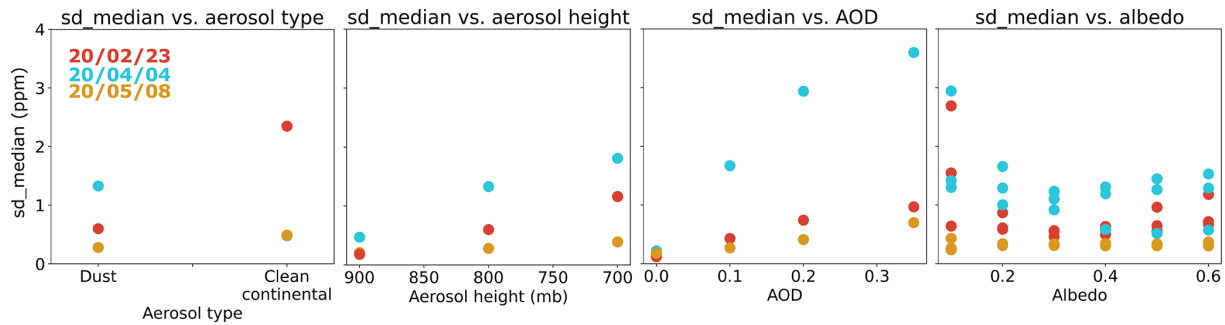


**Figure 17.**  $sd\_median$  versus each of our tested parameters.

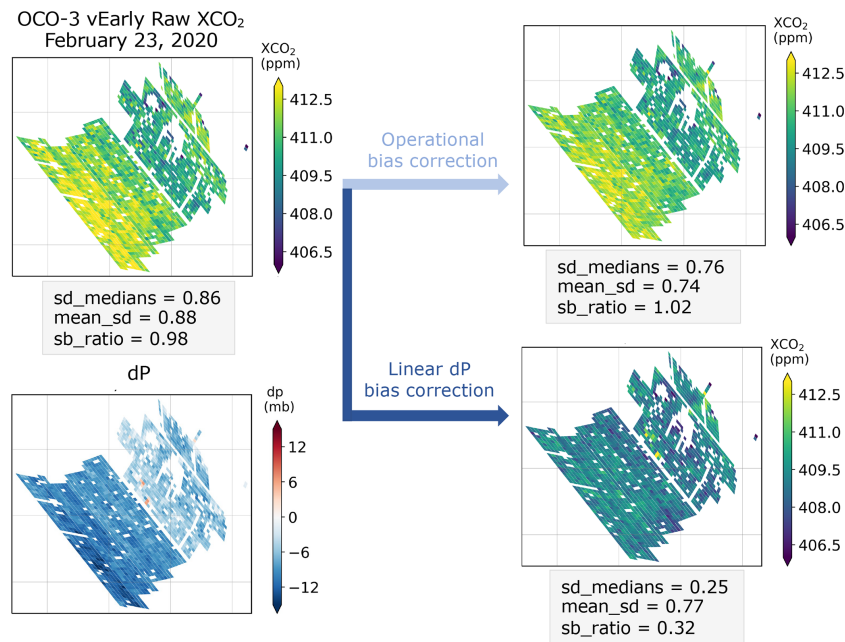


**Figure 18.** 23 February 2020 vEarly SAM from OCO-3, showing the effects of the operational bias correction and a linear dP-derived bias correction on the observed SB. The linear dP bias correction is more similar to the bias correction in v10.

vEarly operational bias correction. Figure 18 shows this phenomenon for the 23 February vEarly data. This may make some sense relative to our simulation results, which show that aerosol properties have the most influence on SB: the retrieval might account for complex aerosol effects by over-correcting surface pressure. Some, but not all, of our simulation configurations did show a similar correlation between dP and  $X_{CO_2}$ . Thus the improved dP correction seems likely to improve SB, via mitigation of aerosol effects, in some scenes but not all. The dP bias correction in v10 will be more effective generally than in vEarly, because the dP correction assumes accurate prior surface pressures, which is not the case in the presence of the significant geolocation errors suffered in vEarly.

For our comparison between v10 and vEarly, we evaluate a total of 5459 SAMs from v10 (specifically, version B10306r; OCO-2/OCO-3 Science Team et al., 2022) that have vEarly

counterparts. These SAMs span from August 2019 to June 2021. For the most direct comparison, we first apply the more restrictive v10 sounding selection criteria to vEarly. We apply quality filtering and bias correction, narrow down to only SAMs with at least 500 soundings ( $N > 500$  representing the number of soundings, NSAM representing the number of  $N > 500$  SAMs), and calculate our SB parameters from Eq. (1). vEarly quality filtering is our custom  $|dP_{abp}| < 16$  hPa filter, and v10 is filtered using the operational v10 quality flags. Figure 19 details the comparison.

Recall from Sect. 3 that  $sb\_ratio$  is the result of dividing  $sd\_median$  by  $mean\_sd$ , where  $sd\_median$  is essentially a measure of swath-to-swath bias and  $mean\_sd$  a measure of within-swath – or within-scene – noise. Figure 19 shows that the swath-to-swath bias is greatly decreased with filtering and bias correction in v10; the same is true of the noise within-swath noise. We conclude that swath bias in v10 looks

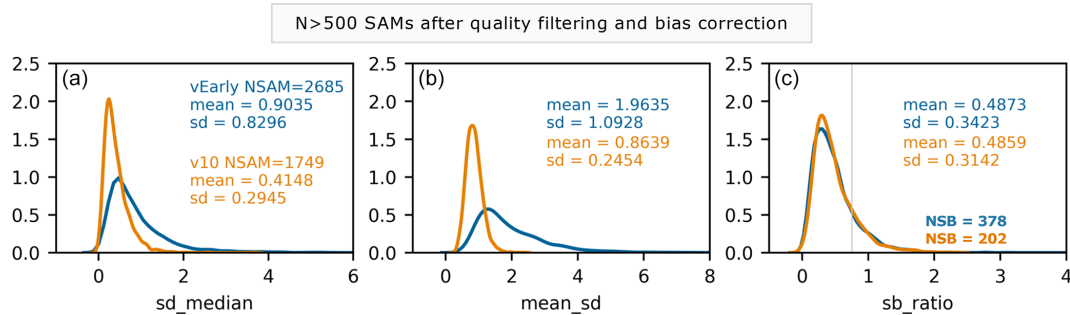


**Figure 19.** Normalized histograms of swath bias parameters for vEarly and v10 SAMs, using v10 sounding selection for both datasets. All SAMs have at least 500 soundings ( $N > 500$ ). The number of SAMs in each dataset is given by NSAM. vEarly is in blue, v10 is in orange, and the SB threshold of  $sb\_ratio > 0.75$  is indicated by the gray line. The number of swath bias cases is listed as NSB in panel (c).

distinctly different than in vEarly: the magnitude is much smaller and exists within a much smoother  $X_{CO_2}$  field. The distribution of the  $sb\_ratio$  does look similar to vEarly, but there are fewer SAMs with SB in v10. Quality filtering in v10 decreases the number of  $N > 500$  SAMs fairly significantly, which we believe is a more realistic result than the more permissive  $dP\_abp$  filtering used for vEarly. Per this exercise, out of the full 5459 SAMs compared, vEarly contains 6.9 % SB cases, compared to only 3.7 % in v10.

Quality filtering and bias correction each have their own effect on the swath bias, and improvements due specifically to the v10 bias correction could be derived either from the improved  $dP$  correction or the new weak  $CO_2$  albedo correction, although we suspect the  $dP$  term as previously discussed. To separate these effects, we apply each of the v10 parametric bias correction terms to the raw  $X_{CO_2}$  data individually and evaluate the change in SB strength (defined as the  $sb\_ratio$  from Eq. 1). We perform this test for a subset of 475 cases with  $sb\_flag = 1$  in the raw v10 data. Figure 20 shows the results of this exercise.

The  $dP$  correction indeed has the largest impact in reducing SB, in line with our hypotheses regarding both aerosol effects and geolocation. The median SAM's SB is weakened by 20 % with this bias correction term applied. The weak  $CO_2$  albedo correction has a much smaller effect on SB overall, with a median SB change of  $-1\%$ . Other bias correction terms have a similarly minor effect on SB compared to  $dP$ , and the full bias correction with all terms applied reduces SB in most SAMs, with a median SB change of  $-16.5\%$ . We do note, however, that in tests applying the bias correction and quality filtering separately, the quality filtering had a more substantial effect on SB: bias correction alone reduced the number of v10 SB SAMs from 325 (in raw data) to 310, and quality filtering reduced it from 325 to 225. While  $dP$  had the largest impact within the bias correction, the quality filtering had an even larger impact, indicating that the swath bias is not driven specifically by  $dP$  but rather by extreme aerosol effects being characterized poorly within the retrieval.

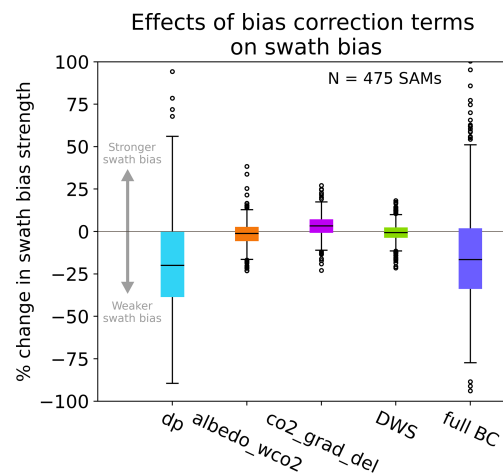


**Figure 20.** SB response to individual v10 bias correction terms for 475 v10 SAMs whose  $sb\_flag = 1$  prior to filtering and bias correction. This set of SAMs extends beyond the time period used in the vEarly comparison.

All three of the Australian ECOSTRESS SAMs used in our simulation work benefit from v10 improvements. Figure 21 shows a comparison between their vEarly and v10 bias-corrected and quality-filtered counterparts. None of these cases are flagged as having SB in v10, all with  $sb\_ratios$  less than 0.75. Between the three, several v10 improvements are apparent.

In the 23 February SAM, geolocation and calibration improvements remove the across-swath gradient almost entirely, and improved quality flags also remove many soundings where we retrieve higher aerosol optical depths. On 4 April, improved geolocation and bias correction sharpen a few thin topographical features stretching northwest to southeast, indicating a topography effect such as those described in (Kiel et al., 2019). A footprint-dependent bias is also removed by bias correction in v10 – we see the same bias improved in the 8 May SAM. On 8 May the v10 bias correction also removes a signal in the northeast corner of

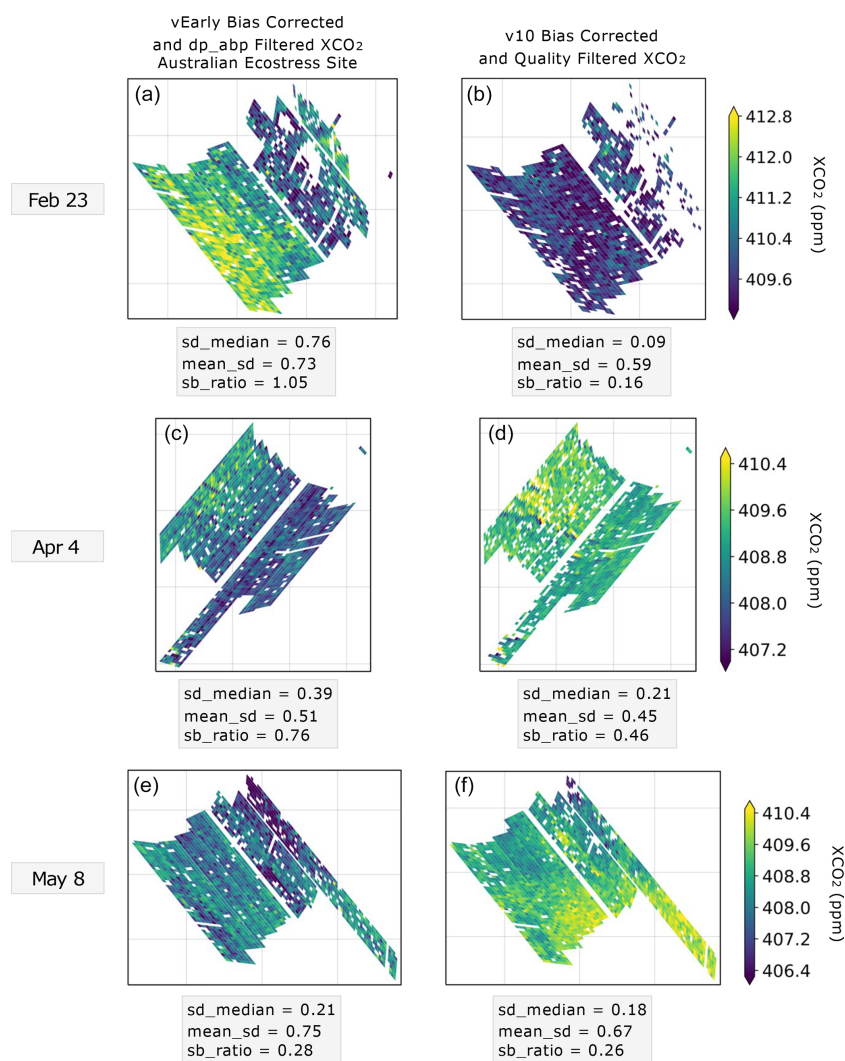


**Figure 21.** The three Australian SAMs used in our simulation work, comparing the operational products from vEarly (a, c, e) and v10 (b, d, f).

the SAM, which we believe is related to a real aerosol signal manifesting in dP, per MAIAC data over the site. The sb<sub>ratio</sub> is reduced in v10 for all three SAMs.

Aside from our three Australian SAMs, we perform some visual analysis of 243 quality-filtered, bias-corrected SB SAMs from the v10 dataset, extending through October 2021. In an attempt to estimate how many of these SAMs seem to suffer from a genuine geometry-related SB and how many simply contain across-swath XCO<sub>2</sub> gradients derived from other sources, we look at maps of raw XCO<sub>2</sub>, bias-corrected and quality-filtered XCO<sub>2</sub>, dP, retrieved albedo, and TROPOMI NO<sub>2</sub> (Veefkind et al., 2012; Van Geffen et al., 2019). We estimate that at least half of the 243 SAMs are flagged as SB cases due to XCO<sub>2</sub> variability caused not by geometry or aerosol effects, but by other biases (e.g., topography, albedo); real XCO<sub>2</sub> signals, including some with fossil signals which are verifiable using TROPOMI NO<sub>2</sub> data; or other unknown sources. An example of fossil emissions trig-

gering a false SB flag is shown in Fig. 22, on the coast of Saudi Arabia. TROPOMI NO<sub>2</sub> indicates a real XCO<sub>2</sub> plume, but despite the v10 quality flags removing a generous number of soundings, enough of the OCO-3 SAM remains after bias correction and filtering to see an across-swath gradient which is derived from the contrast of the fossil fuel signal and background. Figure 23 shows an example of a v10 SAM with true swath bias: both the raw and bias-corrected data show a shift of nearly 1 ppm in XCO<sub>2</sub> between swaths, which may drown out any existing fossil signal as observed by TROPOMI NO<sub>2</sub>. The swath bias appears to be due to higher aerosol loading in the scene, with MAIAC indicating AODs of nearly 0.3.

We acknowledge that vEarly suffers from the same limitations as v10 in terms of this interpretation of the sb<sub>flag</sub>, indicating that vEarly likely also suffers from a far smaller number of true SB cases than our flag suggests. Despite this, we still consider v10 an improvement based on the across-swath

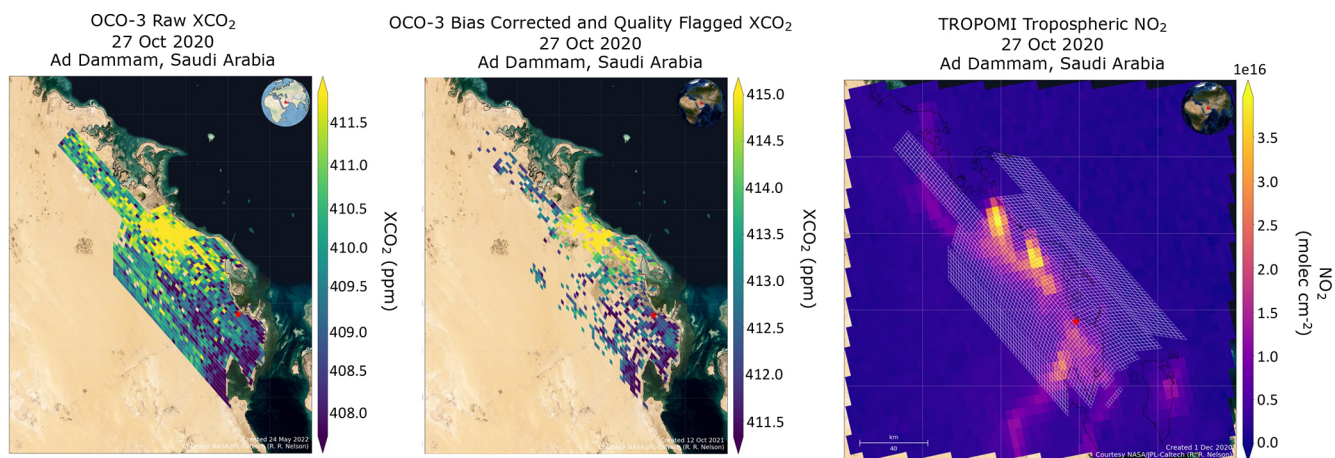


**Figure 22.** A v10 OCO-3 SAM whose SB flag is triggered by a real across-swath  $X_{\text{CO}_2}$  gradient due to a fossil fuel emission signal clustered on one side of the SAM, rather than a geometry-related bias.

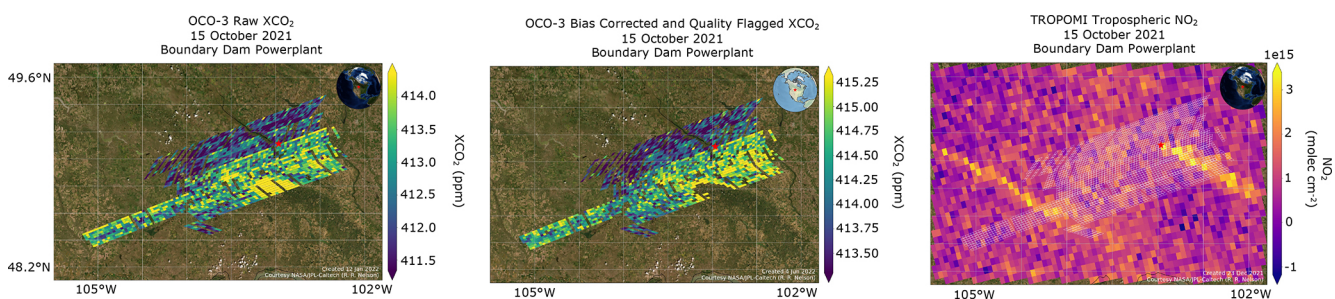


**Figure 23.** A v10 OCO-3 SAM at Boundary Dam power plant in Saskatchewan, Canada, which appears to have a true swath bias, even after bias correction and quality filtering. The SAM was taken at 16:42 UTC (10:42 LT), and MODIS data indicate high AODs of around 0.3 in the area on this date.

and within-swath improvements to the  $X_{\text{CO}_2}$  field shown in Fig. 19.

There is a small number of SB-affected SAMs in v10 which are not flagged as such in vEarly, which we find is due to a less noisy  $X_{\text{CO}_2}$  field overall – that is, a reduction in the denominator of Eq. (1). We do not believe most of these cases suffer from significant SB. Overall, SB appears to be driven primarily by aerosol effects, and as shown in Sect. 6, our retrieval generates its own SB in certain instances. However, v10 quality filters prove especially effective at mitigating swath biases, and the dP term in the v10 bias correction appears to remove some SB even after quality filtering because of the way aerosol effects are often folded into dP. Therefore, while it still exists, filtering and bias correction largely appear to mitigate SB in OCO-3 v10 data.

## 8 Conclusions

Target mode data from the OCO-2 and OCO-3 missions, and SAM data from OCO-3, provide us with an avenue to explore not only local-scale  $\text{CO}_2$  emissions but also geometry-related

biases in space-based  $\text{CO}_2$  measurements, since they sample a nearly instantaneous atmosphere from a range of viewing angles. With the arrival of the first operational OCO-3 SAM data, we observe a new geometry-related bias in the form of a swath-dependent  $X_{\text{CO}_2}$  gradient spanning several parts per million. We refer to this as swath bias.

In this study we develop a set of criteria to detect swath bias (SB) in any given SAM by calculating the ratio of swath-to-swath scatter in the  $X_{\text{CO}_2}$  field to the scatter over the full scene and triggering a swath bias flag (`sb_flag`) over a threshold value of 0.75 (Eq. 1). Per these criteria, we find that roughly 12 % of SAMs in the vEarly dataset suffer from SB, and 256 of those 352 cases are over urban/fossil sites. An analysis of key retrieval parameters reveals a relationship between SB and local time of day, correlated to solar zenith angle. Together these describe a correlation to path length, which could be related to viewing and solar geometry, as well as aerosol optical depth – and we do observe a higher fraction of SB at SAMs with higher retrieved optical depths. There is also a higher frequency of SAMs over scenes with higher retrieved albedo. We turn to the L1b simulator framework to study these relationships in a more systematic manner.

By studying real OCO-3 SAMs, we show that SB in  $X_{\text{CO}_2}$  is primarily correlated to the viewing geometry, though the geometry signal in other retrieved parameters appears easily obscured by signals from other sources, such as heterogeneous aerosol fields or surface topography. To remove additional in-scene variability, we build custom aerosol and surface scenes to generate simulated radiance spectra and use those spectra to retrieve  $X_{\text{CO}_2}$  with the ACOS L2FP algorithm. Our first tests show that we can successfully reproduce geometry-driven SB effects via this method, and while not identical to the observed vEarly SB, the similarities are enough to instill confidence in the utility of the procedure. We select a set of three SAMs over an Australian desert site, which represent a range of solar zenith angles and viewing geometries, as well as a range of SB effects. For these three SAMs, we perform a series of controlled tests, changing individual inputs to the simulated scene.

Scenes with no aerosol show little to no SB, but each SAM's response to aerosol height and optical depth is consistent – the higher the aerosol within the column, or the higher the AOD, the stronger the SB. We test one coarse and one fine mode aerosol for each SAM, and each produces a different SB, but which is stronger depends on the conditions of the SAM. The precise combination of geometry and aerosol optical properties required for a strong SB appears to be complex; although it is apparent that the unique optical properties of each aerosol type interact with the geometry to produce the different  $X_{\text{CO}_2}$  patterns. The exact nature of these interactions would require further study to describe in a quantitative manner.

Our manipulation of surface albedo, testing a range of values from 0.1 to 0.6 in each of the three OCO-3 bands, reveals that swath bias is more likely to occur over dark surfaces with low albedos. Our O<sub>2</sub> A-band filter is skilled at mitigating the effect over dark surfaces, however, where aerosols are differentiable from the surface beneath. It has more trouble discerning aerosols and their effects over bright surfaces and is less likely to filter out affected soundings. We believe this behavior may account for the observed trend of more SB SAMs at higher albedos in vEarly and reinforces the fact that SB is intimately linked to aerosols.

Finally, we replicate our vEarly analysis using the updated version 10 dataset and see vastly improved statistics. We find that improved quality filtering is the primary driver of this development, removing a significant number of soundings in SB-affected SAMs. Better sounding selection and significant geolocation improvements, combined with a better dP bias correction, also make v10 more effective at mitigating SB effects and generally improve the quality of the final data product. We estimate that at least half of the remaining v10 SB SAMs, after filtering and bias correction, may in fact be triggered by other biases or real  $X_{\text{CO}_2}$  signals, but further investigation is required to quantify these numbers accurately. For the remaining truly geometry-related SB, we hypothesize that retrieval algorithm adjustments, with increased complex-

ity or better prior aerosol information, may help mitigate the SB signal in the final Level 2 product. Some remaining SB may also be due to small remaining OCO-3 geolocation errors, improvements to which are being pursued in future data versions and may address this issue; additionally, alternate or supplemental postprocessing may prove effective. We leave these approaches to future study.

We conclude that the swath bias effect is intrinsically linked to the presence of aerosols, their interplay with observation geometry, and our ability to filter out aerosol-affected soundings, as well as the way aerosols are characterized within our retrieval. There has long been room for improvement in the latter, and it is a critical piece of the retrieval puzzle with further complexity to be studied. Work by Rusli et al. (2021), in support of the European Space Agency's CO<sub>2</sub> Monitoring (CO2M) mission (Ciais et al., 2017; Janssens-Maenhout et al., 2020), showed with synthetic data that jointly retrieving  $X_{\text{CO}_2}$  and aerosol information provided by a multi-angle polarimeter (MAP) can significantly improve aerosol-related biases, overall bias, and spread in the resulting  $X_{\text{CO}_2}$ . Strategies along these lines – complementary, aerosol-dedicated instruments alongside spectrometers measuring trace gases – may be one effective approach to improving the biases we see in this study. Accurately representing aerosols in greenhouse gas retrievals will prove just as important to future CO<sub>2</sub>-monitoring missions as it has to OCO-3 – perhaps even more so as the remote sensing community continues to hone in on local-scale emissions.

*Code and data availability.* OCO-3 Level 2 files are available at the NASA GES DISC (<https://doi.org/10.5067/970BCC4DHH24>, OCO-2/OCO-3 Science Team et al., 2022). Version 10.3 (B10306r, specifically) is used in this study, which is nearly identical to Version 10.4 on the GES DISC, apart from a small time-dependent correction which does not affect the few-minute variations we analyze here. B10306r files are available upon request. CarbonTracker CT2019B is available through NOAA GML at [https://gml.noaa.gov/aftp/products/carbontracker/co2/CT2019B/molefractions/co2\\_total/](https://gml.noaa.gov/aftp/products/carbontracker/co2/CT2019B/molefractions/co2_total/) (last access: 25 July 2022; Jacobson et al., 2020). NCEP-NCAR Reanalysis 1 meteorological data are provided by the NOAA PSL in Boulder, Colorado, and are found at <https://psl.noaa.gov/data/gridded/data.ncep.reanalysis.html> (last access: 25 July 2022; NOAA/NCEP, 2022). The MODIS MCD43A1 product is at <https://doi.org/10.5067/MODIS/MCD43A1.006> (Schaaf and Wang, 2015). The left panel and insets of Fig. 3 were created using visualization software developed at CSU/CIRA by Heather Cronk, the code for which is available at <https://doi.org/10.5281/zenodo.7517017> (Cronk et al., 2023).

*Author contributions.* EB completed the bulk of the analysis and wrote the initial draft of the published work. CWO'D further advised on retrieval behavior, scientific direction, and methodology and acquired funding for this work. TET served as a mentor on the software side and contributed data, retrieval, and scientific guidance. AM also provided key input on retrieval algorithm behavior

and scientific analysis. RRN assisted with case selection, lent data- and retrieval-related expertise, and contributed a myriad of figures. MK provided data and retrieval insights; AE guided the focus of this work, along with that of the OCO-3 mission; and RR and BF were (and are) crucial to the development and record of the latest and greatest OCO-3 data products. All authors contributed to the editing of the paper.

*Competing interests.* The contact author has declared that none of the authors has any competing interests.

*Disclaimer.* Publisher's note: Copernicus Publications remains neutral with regard to jurisdictional claims in published maps and institutional affiliations.

*Acknowledgements.* The authors would like to thank the OCO-3 science team at large for making the most of such an impactful, yet relatively brief, mission. Additional thanks to Greg McGarragh, Peter Somkuti, and Heather Cronk for their assistance with retrieval infrastructure, software questions, and data visualization.

*Financial support.* This research has been supported by the National Aeronautics and Space Administration (grant nos. 80NSSC21K1078 and 1557985).

*Review statement.* This paper was edited by Frank Hase and reviewed by two anonymous referees.

## References

- Aben, I., Hasekamp, O., and Hartmann, W.: Uncertainties in the space-based measurements of CO<sub>2</sub> columns due to scattering in the Earth's atmosphere, *J. Quant. Spectrosc. Ra.*, 104, 450–459, <https://doi.org/10.1016/j.jqsrt.2006.09.013>, 2007.
- Basilio, R. R., Bennett, M. W., Eldering, A., Lawson, P. R., and Rosenberg, R. A.: Orbiting Carbon Observatory-3 (OCO-3), remote sensing from the International Space Station (ISS), in: *Sensors, Systems, and Next-Generation Satellites XXIII*, International Society for Optics and Photonics, vol. 11151, 1115109, <https://doi.org/10.1117/12.2534996>, 2019.
- Bertaux, J.-L., Hauchecorne, A., Lefèvre, F., Bréon, F.-M., Blanot, L., Jouglet, D., Lafrique, P., and Akaev, P.: The use of the 1.27 μm O<sub>2</sub> absorption band for greenhouse gas monitoring from space and application to MicroCarb, *Atmos. Meas. Tech.*, 13, 3329–3374, <https://doi.org/10.5194/amt-13-3329-2020>, 2020.
- Bösch, H., Toon, G. C., Sen, B., Washenfelder, R. A., Wennberg, P. O., Buchwitz, M., de Beek, R., Burrows, J. P., Crisp, D., Christi, M., Connor, B. J., Natraj, V., and Yung, Y. L.: Space-based near-infrared CO<sub>2</sub> measurements: Testing the Orbiting Carbon Observatory retrieval algorithm and validation concept using SCIAMACHY observations over Park Falls, Wisconsin, *J. Geophys. Res.-Atmos.*, 111, D23302, <https://doi.org/10.1029/2006JD007080>, 2006.
- Bovensmann, H., Burrows, J., Buchwitz, M., Frerick, J., Noel, S., Rozanov, V., Chance, K., and Goede, A.: SCIAMACHY: Mission objectives and measurement modes, *J. Atmos. Sci.*, 56, 127–150, 1999.
- Buchwitz, M., Schneising, O., Burrows, J. P., Bovensmann, H., Reuter, M., and Notholt, J.: First direct observation of the atmospheric CO<sub>2</sub> year-to-year increase from space, *Atmos. Chem. Phys.*, 7, 4249–4256, <https://doi.org/10.5194/acp-7-4249-2007>, 2007.
- Butz, A., Hasekamp, O. P., Frankenberg, C., and Aben, I.: Retrievals of atmospheric CO<sub>2</sub> from simulated space-borne measurements of backscattered near-infrared sunlight: accounting for aerosol effects, *Appl. Optics*, 48, 3322–3336, 2009.
- Ciais, P., Palmer, P., Scholze, M., Kentarchos, A., Brunhes, T., Dolman, H., Husband, R., Holmlund, K., Engelen, R., Janssens-Maenhout, G., Zunker, H., Denier van der Gon, H., Drinkwater, M., Pinty, B., Meijer, Y., Heimann, M., and Dowell, M.: An operational anthropogenic CO<sub>2</sub> emissions monitoring & verification system: baseline requirements, model components and functional architecture, European Commission and Joint Research Centre, <https://doi.org/10.2760/08644>, 2017.
- Connor, B., Bösch, H., McDuffie, J., Taylor, T., Fu, D., Frankenberg, C., O'Dell, C., Payne, V. H., Gunson, M., Pollock, R., Hobbs, J., Oyafuso, F., and Jiang, Y.: Quantification of uncertainties in OCO-2 measurements of XCO<sub>2</sub>: simulations and linear error analysis, *Atmos. Meas. Tech.*, 9, 5227–5238, <https://doi.org/10.5194/amt-9-5227-2016>, 2016.
- Crisp, D., Pollock, H. R., Rosenberg, R., Chapsky, L., Lee, R. A. M., Oyafuso, F. A., Frankenberg, C., O'Dell, C. W., Bruegge, C. J., Doran, G. B., Eldering, A., Fisher, B. M., Fu, D., Gunson, M. R., Mandrake, L., Osterman, G. B., Schwandner, F. M., Sun, K., Taylor, T. E., Wennberg, P. O., and Wunch, D.: The on-orbit performance of the Orbiting Carbon Observatory-2 (OCO-2) instrument and its radiometrically calibrated products, *Atmos. Meas. Tech.*, 10, 59–81, <https://doi.org/10.5194/amt-10-59-2017>, 2017.
- Cronk, H., Merrelli, A., and Tkachev, M.: hcronk/oco\_vistool: Initial official release (v1.0.0), Zenodo [code], <https://doi.org/10.5281/zenodo.7517017>, 2023.
- Dubovik, O., Holben, B., Eck, T. F., Smirnov, A., Kaufman, Y. J., King, M. D., Tanré, D., and Slutsker, I.: Variability of absorption and optical properties of key aerosol types observed in worldwide locations, *J. Atmos. Sci.*, 59, 590–608, 2002.
- Eldering, A., O'Dell, C. W., Wennberg, P. O., Crisp, D., Gunson, M. R., Viatte, C., Avis, C., Braverman, A., Castano, R., Chang, A., Chapsky, L., Cheng, C., Connor, B., Dang, L., Doran, G., Fisher, B., Frankenberg, C., Fu, D., Granat, R., Hobbs, J., Lee, R. A. M., Mandrake, L., McDuffie, J., Miller, C. E., Myers, V., Natraj, V., O'Brien, D., Osterman, G. B., Oyafuso, F., Payne, V. H., Pollock, H. R., Polonsky, I., Roehl, C. M., Rosenberg, R., Schwandner, F., Smyth, M., Tang, V., Taylor, T. E., To, C., Wunch, D., and Yoshimizu, J.: The Orbiting Carbon Observatory-2: first 18 months of science data products, *Atmos. Meas. Tech.*, 10, 549–563, <https://doi.org/10.5194/amt-10-549-2017>, 2017.
- Eldering, A., Taylor, T. E., O'Dell, C. W., and Pavlick, R.: The OCO-3 mission: measurement objectives and expected performance based on 1 year of simulated data, *Atmos.*

- Meas. Tech., 12, 2341–2370, <https://doi.org/10.5194/amt-12-2341-2019>, 2019.
- Frankenberg, C., Hasekamp, O., O'Dell, C., Sanghavi, S., Butz, A., and Worden, J.: Aerosol information content analysis of multi-angle high spectral resolution measurements and its benefit for high accuracy greenhouse gas retrievals, *Atmos. Meas. Tech.*, 5, 1809–1821, <https://doi.org/10.5194/amt-5-1809-2012>, 2012.
- Gelaro, R., McCarty, W., Suárez, M. J., Todling, R., Molod, A., Takacs, L., Randles, C. A., Darmenov, A., Bosilovich, M., Reichle, R., Wargan, K., Coy, L., Cullather, R., Draper, C., Akella, S., Buchard, V., Conaty, A., da Silva, A., Gu, W., Kim, G., Koster, R., Lucchesi, R., Merkova, D., Nielsen, J., Partyka, G., Pawson, S., Putman, W., Rienecker, M., Schubert, S., Sienkiewicz, M., and Zhao, B.: The modern-era retrospective analysis for research and applications, version 2 (MERRA-2), *J. Climate*, 30, 5419–5454, 2017.
- Hakkarainen, J., Ialongo, I., and Tamminen, J.: Direct space-based observations of anthropogenic CO<sub>2</sub> emission areas from OCO-2, *Geophys. Res. Lett.*, 43, 11400–11406, <https://doi.org/10.1002/2016GL070885>, 2016.
- Jacobson, A., Schuldt, K., Miller, J., Oda, T., Tans, P., Andrews, A., Mund, J., Ott, L., Collatz, G., Aalto, T., Afshar, S., Aikin, K., Aoki, S., Apadula, F., Baier, B., Bergamaschi, P., Beyersdorf, A., Biraud, S., Bollenbacher, A., Bowling, D., Brailsford, G., Abshire, J., Chen, G., Huilin, C., Lukasz, C., Sites, C., Colomb, A., Conil, S., Cox, A., Cristofanelli, P., Cuevas, E., Curcoll, R., Sloop, C. D., Davis, K., Wekker, S., Delmotte, M., DiGangi, J., Dlugokencky, E., Ehleringer, J., Elkins, J., Emmenegger, L., Fischer, M., Forster, G., Frumau, A., Galkowski, M., Gatti, L., Gloor, E., Griffis, T., Hammer, S., Haszpra, L., Hatakka, J., Heliasz, M., Hensen, A., Hermanssen, O., Hintsa, E., Holst, J., Jaffe, D., Karion, A., Kawa, S., Keeling, R., Keronen, P., Kolarik, P., Kominkova, K., Kort, E., Krummel, P., Kubistin, D., Labuschagne, C., Langenfelds, R., Laurent, O., Laurila, T., Lauvaux, T., Law, B., Lee, J., Lehner, I., Leuenberger, M., Levin, I., Levula, J., Lin, J., Lindauer, M., Loh, Z., Lopez, M., Luijkx, I., Lund Myhre, C., Machida, T., Mammarella, I., Manca, G., Manning, A., Manning, A., Marek, M., Marklund, P., Martin, M., Matsuueda, H., McKain, K., Meijer, H., Meinhardt, F., Miles, N., Miller, C., Mölder, M., Montzka, S., Moore, F., Morgui, J.-A., Morimoto, S., Munger, B., Necki, J., Newman, S., Nichol, S., Niwa, Y., O'Doherty, S., Ottosson-Löfvenius, M., Paplawsky, B., Peischl, J., Peltola, O., Pichon, J.-M., Piper, S., Plass-Dölmer, C., Ramonet, M., Reyes-Sanchez, E., Richardson, S., Riris, H., Ryerson, T., Saito, K., Sargent, M., Sasakawa, M., Sawa, Y., Say, D., Scheeren, B., Schmidt, M., Schmidt, A., Schumacher, M., Shepson, P., Shook, M., Stanley, K., Steinbacher, M., Stephens, B., Sweeney, C., Thoning, K., Torn, M., Turnbull, J., Tørseth, K., Bulk, P., Dinter, D., Vermeulen, A., Viner, B., Vitkova, G., Walker, S., Weyrauch, D., Wofsy, S., Worthy, D., Young, D., and Zimnoc, M.: CarbonTracker CT2019B, NOAA Earth System Research Laboratory, Global Monitoring Division [data set], <https://doi.org/10.25925/20201008>, 2020 (data available at: [https://gml.noaa.gov/aftp/products/carbontracker/co2/CT2019B/molefractions/co2\\_total/](https://gml.noaa.gov/aftp/products/carbontracker/co2/CT2019B/molefractions/co2_total/), last access: 25 July 2022).
- Janssens-Maenhout, G., Pinty, B., Dowell, M., Zunker, H., Anderson, E., Balsamo, G., Bézy, J.-L., Brunhes, T., Bösch, H., Bojkov, B., Brunner, D., Buchwitz, M., Crisp, D., Ciais, P., Counet, P., Dee, D., Denier van der Gon, H., Dolman, H., Drinkwater, M., Dubovik, O., Engelen, R., Fehr, T., Fernandez, V., Heimann, M., Holmlund, K., Houweling, S., Husband, R., Juvyns, O., Kentarchos, A., Landgraf, J., Lang, R., Löscher, A., Marshall, J., Meijer, Y., Nakajima, M., Palmer, P., Peylin, P., Rayner, P., Scholze, M., Sierk, B., Tamminen, J., and Veefkind, P.: Toward an Operational Anthropogenic CO<sub>2</sub> Emissions Monitoring and Verification Support Capacity, *B. Am. Meteorol. Soc.*, 101, E1439–E1451, 2020.
- Kalnay, E., Kanamitsu, M., Kistler, R., Collins, W., Deaven, D., Gandin, L., Iredell, M., Saha, S., White, G., Woollen, J., Zhu, Y., Chelliah, M., Ebisuzaki, W., Higgins, W., Janowiak, J., Mo, K., Ropelewski, C., Wang, J., Leetmaa, A., Reynolds, R., Jenne, R., and Joseph, D.: The NCEP/NCAR 40-Year Reanalysis Project, *B. Am. Meteorol. Soc.*, 77, 437–472, [https://doi.org/10.1175/1520-0477\(1996\)077<0437:TNYRP>2.0.CO;2](https://doi.org/10.1175/1520-0477(1996)077<0437:TNYRP>2.0.CO;2), 1996.
- Kasahara, M., Kachi, M., Inaoka, K., Fujii, H., Kubota, T., Shimada, R., and Kojima, Y.: Overview and current status of GOSAT-GW mission and AMSR3 instrument, in: *Sensors, Systems, and Next-Generation Satellites XXIV, SPIE Remote Sensing, SPIE*, vol. 11530, 1153007, <https://doi.org/10.1117/12.2573914>, 2020.
- Kiel, M., O'Dell, C. W., Fisher, B., Eldering, A., Nassar, R., MacDonald, C. G., and Wennberg, P. O.: How bias correction goes wrong: measurement of X<sub>CO<sub>2</sub></sub> affected by erroneous surface pressure estimates, *Atmos. Meas. Tech.*, 12, 2241–2259, <https://doi.org/10.5194/amt-12-2241-2019>, 2019.
- Kiel, M., Eldering, A., Roten, D., Lin, J., Feng, S., Lei, R., Lauvaux, T., Oda, T., Roehl, C., Blavier, J.-F., and Iraci, L.: Urban-focused satellite CO<sub>2</sub> observations from the Orbiting Carbon Observatory-3: A first look at the Los Angeles megacity, *Remote Sens. Environ.*, 258, 112314, <https://doi.org/10.1016/j.rse.2021.112314>, 2021.
- Kuze, A., Suto, H., Nakajima, M., and Hamazaki, T.: Thermal and near infrared sensor for carbon observation Fourier-transform spectrometer on the Greenhouse Gases Observing Satellite for greenhouse gases monitoring, *Appl. Optics*, 48, 6716–6733, 2009.
- Lyapustin, A., Wang, Y., Laszlo, I., Kahn, R., Korkin, S., Remer, L., Levy, R., and Reid, J.: Multiangle implementation of atmospheric correction (MAIAC): 2. Aerosol algorithm, *J. Geophys. Res.-Atmos.*, 116, D03211, <https://doi.org/10.1029/2010JD014986>, 2011.
- MODIS Land Science Team: MODIS/Terra+Aqua Land Aerosol Optical Depth Daily L2G Global 1km SIN Grid, NASA LANCE MODIS at the MODAPS [data set], <https://doi.org/10.5067/MODIS/MCD19A2N.NRT.006>, 2019.
- Moore III, B., Crowell, S. M., Rayner, P. J., Kumer, J., O'Dell, C. W., O'Brien, D., Utembe, S., Polonsky, I., Schimel, D., and Lemen, J.: The potential of the Geostationary Carbon Cycle Observatory (GeoCarb) to provide multi-scale constraints on the carbon cycle in the Americas, *Front. Environ. Sci.*, 6, <https://doi.org/10.3389/fenvs.2018.00109>, 2018.
- Nassar, R., Hill, T. G., McLinden, C. A., Wunch, D., Jones, D. B. A., and Crisp, D.: Quantifying CO<sub>2</sub> Emissions From Individual Power Plants From Space, *Geophys. Res. Lett.*, 44, 10045–10053, <https://doi.org/10.1002/2017GL074702>, 2017.
- Nassar, R., Mastrogiacomo, J.-P., Bateman-Hemphill, W., McCracken, C., MacDonald, C. G., Hill, T., O'Dell, C. W., Kiel, M., and Crisp, D.: Advances in quantifying power plant CO<sub>2</sub>

- emissions with OCO-2, *Remote Sens. Environ.*, 264, 112579, <https://doi.org/10.1016/j.rse.2021.112579>, 2021.
- Nelson, R. R. and O'Dell, C. W.: The impact of improved aerosol priors on near-infrared measurements of carbon dioxide, *Atmos. Meas. Tech.*, 12, 1495–1512, <https://doi.org/10.5194/amt-12-1495-2019>, 2019.
- Nivitanont, J., Crowell, S. M. R., and Moore III, B.: A scanning strategy optimized for signal-to-noise ratio for the Geostationary Carbon Cycle Observatory (GeoCarb) instrument, *Atmos. Meas. Tech.*, 12, 3317–3334, <https://doi.org/10.5194/amt-12-3317-2019>, 2019.
- NOAA/NCEP: NCEP/NCAR Reanalysis 1, NOAA PSL, Boulder, Colorado [data set], <https://psl.noaa.gov/data/gridded/data.ncep.reanalysis.html>, last access: 25 July 2022.
- O'Brien, D., Polonsky, I., O'Dell, C., and Carhedan, A.: Orbiting Carbon Observatory (OCO), Algorithm Theoretical Basis Document: The OCO simulator, Tech. rep., Cooperative Institute for Research in the Atmosphere, Colorado State University, [https://reef.atmos.colostate.edu/~embell/oco\\_sims/OCO\\_simulator\\_doc.pdf](https://reef.atmos.colostate.edu/~embell/oco_sims/OCO_simulator_doc.pdf) (last access: 8 May 2022), 2009.
- OCO-2/OCO-3 Science Team, Chatterjee, A., and Payne, V.: OCO-3 Level 2 bias-corrected XCO<sub>2</sub> and other select fields from the full-physics retrieval aggregated as daily files, Retrospective processing v10.4r, Greenbelt, MD, USA, Goddard Earth Sciences Data and Information Services Center (GES DISC) [data set], <https://doi.org/10.5067/970BCC4DHH24>, 2022.
- O'Dell, C. W., Connor, B., Bösch, H., O'Brien, D., Frankenberg, C., Castano, R., Christi, M., Eldering, D., Fisher, B., Gunson, M., McDuffie, J., Miller, C. E., Natraj, V., Oyafuso, F., Polonsky, I., Smyth, M., Taylor, T., Toon, G. C., Wennberg, P. O., and Wunch, D.: The ACOS CO<sub>2</sub> retrieval algorithm – Part 1: Description and validation against synthetic observations, *Atmos. Meas. Tech.*, 5, 99–121, <https://doi.org/10.5194/amt-5-99-2012>, 2012.
- O'Dell, C. W., Eldering, A., Wennberg, P. O., Crisp, D., Gunson, M. R., Fisher, B., Frankenberg, C., Kiel, M., Lindqvist, H., Mandrake, L., Merrelli, A., Natraj, V., Nelson, R. R., Osterman, G. B., Payne, V. H., Taylor, T. E., Wunch, D., Drouin, B. J., Oyafuso, F., Chang, A., McDuffie, J., Smyth, M., Baker, D. F., Basu, S., Chevallier, F., Crowell, S. M. R., Feng, L., Palmer, P. I., Dubey, M., García, O. E., Griffith, D. W. T., Hase, F., Iraci, L. T., Kivi, R., Morino, I., Notholt, J., Ohyama, H., Petri, C., Roehl, C. M., Sha, M. K., Strong, K., Sussmann, R., Te, Y., Uchino, O., and Velazco, V. A.: Improved retrievals of carbon dioxide from Orbiting Carbon Observatory-2 with the version 8 ACOS algorithm, *Atmos. Meas. Tech.*, 11, 6539–6576, <https://doi.org/10.5194/amt-11-6539-2018>, 2018.
- Osterman, G., O'Dell, C., Eldering, A., Fisher, B., Crisp, D., Cheng, C., Frankenberg, C., Lambert, A., Gunson, M., Mandrake, L., and Wunch, D.: Orbiting Carbon Observatory-2 & 3 Data Product User's Guide, Operational Level 2 Data Version 10 and Lite File Version 10 and vEarly, Tech. rep., Jet Propulsion Laboratory, California Institute of Technology, Colorado State University, University of Toronto, [https://docserver.gesdisc.eosdis.nasa.gov/public/project/OCO/OCO2\\_OCO3\\_B10\\_DUG.pdf](https://docserver.gesdisc.eosdis.nasa.gov/public/project/OCO/OCO2_OCO3_B10_DUG.pdf) (last access: 13 June 2022), 2020.
- Pasternak, F., Bernard, P., Georges, L., and Pascal, V.: The microcarb instrument, in: International Conference on Space Optics – ICSO 2016, Biarritz, France, 25 September 2017, International Society for Optics and Photonics, SPIE, vol. 10562, 485–497, 2017.
- Payne, V. H., Drouin, B. J., Oyafuso, F., Kuai, L., Fisher, B. M., Sung, K., Nemchick, D., Crawford, T. J., Smyth, M., Crisp, D., Adkins, E., Hodges, J. T., Long, D. A., Mlawer, E. J., Merrelli, A., Lunny, E., and O'Dell, C. W.: Absorption coefficient (ABSCO) tables for the Orbiting Carbon Observatories: Version 5.1, *J. Quant. Spectrosc. Ra.*, 255, 107217, <https://doi.org/10.1016/j.jqsrt.2020.107217>, 2020.
- Reuter, M., Buchwitz, M., Schneising, O., Krautwurst, S., O'Dell, C. W., Richter, A., Bovensmann, H., and Burrows, J. P.: Towards monitoring localized CO<sub>2</sub> emissions from space: co-located regional CO<sub>2</sub> and NO<sub>2</sub> enhancements observed by the OCO-2 and S5P satellites, *Atmos. Chem. Phys.*, 19, 9371–9383, <https://doi.org/10.5194/acp-19-9371-2019>, 2019.
- Rienecker, M., Suarez, M., Todling, R., Bacmeister, J., Takacs, L., Liu, H., Gu, W., Sienkiewicz, M., Koster, R., Gelaro, R., Stajner, I., and Nielsen, J.: The GEOS-5 Data Assimilation System: Documentation of Versions 5.0.1, 5.1.0, and 5.2.0, Tech. rep., <https://ntrs.nasa.gov/citations/20120011955> (last access: 25 July 2022), 2008.
- Rißmann, M., Chen, J., Osterman, G., Zhao, X., Dietrich, F., Makowski, M., Hase, F., and Kiel, M.: Comparison of OCO-2 target observations to MUCNet – is it possible to capture urban XCO<sub>2</sub> gradients from space?, *Atmos. Meas. Tech.*, 15, 6605–6623, <https://doi.org/10.5194/amt-15-6605-2022>, 2022.
- Rodgers, C. D.: Inverse methods for atmospheric sounding: theory and practice, vol. 2, World scientific, ISBN 981022740X, 2000.
- Rusli, S. P., Hasekamp, O., van de Brugh, J., Fu, G., Meijer, Y., and Landgraf, J.: Anthropogenic CO<sub>2</sub> monitoring satellite mission: the need for multi-angle polarimetric observations, *Atmos. Meas. Tech.*, 14, 1167–1190, <https://doi.org/10.5194/amt-14-1167-2021>, 2021.
- Schaaf, C. and Wang, Z.: MCD43A1 MODIS/Terra+Aqua BRDF/Albedo Model Parameters Daily L3 Global – 500m V006, NASA EOSDIS Land Processes DAAC [data set], <https://doi.org/10.5067/MODIS/MCD43A1.006>, 2015.
- Schneising, O., Buchwitz, M., Burrows, J. P., Bovensmann, H., Reuter, M., Notholt, J., Macatangay, R., and Warneke, T.: Three years of greenhouse gas column-averaged dry air mole fractions retrieved from satellite – Part 1: Carbon dioxide, *Atmos. Chem. Phys.*, 8, 3827–3853, <https://doi.org/10.5194/acp-8-3827-2008>, 2008.
- Schwandner, F. M., Gunson, M. R., Miller, C. E., Carn, S. A., Eldering, A., Krings, T., Verhulst, K. R., Schimel, D. S., Nguyen, H. M., Crisp, D., O'Dell, C. W., Osterman, G. B., Iraci, L. T., and Podolske, J. R.: Spaceborne detection of localized carbon dioxide sources, *Science*, 358, eaam5782, <https://doi.org/10.1126/science.aam5782>, 2017.
- Tans, P. and Keeling, R.: Annual Mean Growth Rate for Mauna Loa, Hawaii, NOAA/GML, Scripps Institution of Oceanography, <https://gml.noaa.gov/ccgg/trends/gr.html>, last access: 15 June 2022.
- Taylor, T. E., O'Dell, C. W., Frankenberg, C., Partain, P. T., Cronk, H. Q., Savtchenko, A., Nelson, R. R., Rosenthal, E. J., Chang, A. Y., Fisher, B., Osterman, G. B., Pollock, R. H., Crisp, D., Eldering, A., and Gunson, M. R.: Orbiting Carbon Observatory-2 (OCO-2) cloud screening algorithms: validation against collo-

- cated MODIS and CALIOP data, *Atmos. Meas. Tech.*, 9, 973–989, <https://doi.org/10.5194/amt-9-973-2016>, 2016.
- Taylor, T. E., Eldering, A., Merrelli, A., Kiel, M., Somkuti, P., Cheng, C., Rosenberg, R., Fisher, B., Crisp, D., Basilio, R., Bennett, M., Cervantes, D., Chang, A., Dang, L., Frankenberg, C., Haemmerle, V. R., Keller, G. R., Kurosu, T., Laughner, J. L., Lee, R., Marchetti, Y., Nelson, R. R., O'Dell, C. W., Osterman, G., Pavlick, R., Roehl, C., Schneider, R., Spiers, G., To, C., Wells, C., Wennberg, P. O., Yelamanchili, A., and Yu, S.: OCO-3 early mission operations and initial (vEarly) XCO<sub>2</sub> and SIF retrievals, *Remote Sens. Environ.*, 251, 112032, <https://doi.org/10.1016/j.rse.2020.112032>, 2020.
- Torres, A., Keppel-Aleks, G., Doney, S., Fendrock, M., Luis, K., De Mazière, M., Hase, F., Petri, C., Pollard, D., Roehl, C., Sussmann, R., Velazco, V., Warneke, T., and Wunch, D.: A geostatistical framework for quantifying the imprint of mesoscale atmospheric transport on satellite trace gas retrievals, *J. Geophys. Res.-Atmos.*, 124, 9773–9795, 2019.
- Van Geffen, J., Eskes, H., Boersma, K., Maasackers, J., and Veefkind, J.: TROPOMI ATBD of the total and tropospheric NO<sub>2</sub> data products, Tech. rep., <https://docslib.org/doc/12770039/tropomi-atbd-of-the-total-and-tropospheric-no2-data-products> (last access: 26 July 2022), 2019.
- Veefkind, J., Aben, I., McMullan, K., Förster, H., De Vries, J., Otter, G., Claas, J., Eskes, H., de Haan, J., Kleipool, Q., van Weele, M., Hasekamp, O., Hoogeveen, R., Landgraf, J., Snel, R., Tol, P., Ingmann, P., Voors, R., Kruizinga, B., Vink, R., Visser, H., and Levelt, P.: TROPOMI on the ESA Sentinel-5 Precursor: A GMES mission for global observations of the atmospheric composition for climate, air quality and ozone layer applications, *Remote Sens. Environ.*, 120, 70–83, 2012.
- Wang, S., Zhang, Y., Hakkarainen, J., Ju, W., Liu, Y., Jiang, F., and He, W.: Distinguishing Anthropogenic CO<sub>2</sub> Emissions From Different Energy Intensive Industrial Sources Using OCO-2 Observations: A Case Study in Northern China, *J. Geophys. Res.-Atmos.*, 123, 9462–9473, <https://doi.org/10.1029/2018JD029005>, 2018.
- Winker, D. M., Hunt, W. H., and McGill, M. J.: Initial performance assessment of CALIOP, *Geophys. Res. Lett.*, 34, L19803, <https://doi.org/10.1029/2007GL030135>, 2007.
- Worden, J. R., Doran, G., Kulawik, S., Eldering, A., Crisp, D., Frankenberg, C., O'Dell, C., and Bowman, K.: Evaluation and attribution of OCO-2 XCO<sub>2</sub> uncertainties, *Atmos. Meas. Tech.*, 10, 2759–2771, <https://doi.org/10.5194/amt-10-2759-2017>, 2017.
- Wunch, D., Toon, G. C., Blavier, J.-F. L., Washenfelder, R. A., Notholt, J., Connor, B. J., Griffith, D. W., Sherlock, V., and Wennberg, P. O.: The total carbon column observing network, *Philos. T. Roy. Soc. A*, 369, 2087–2112, 2011.
- Wunch, D., Wennberg, P. O., Osterman, G., Fisher, B., Naylor, B., Roehl, C. M., O'Dell, C., Mandrake, L., Viatte, C., Kiel, M., Griffith, D. W. T., Deutscher, N. M., Velazco, V. A., Notholt, J., Warneke, T., Petri, C., De Mazière, M., Sha, M. K., Sussmann, R., Rettinger, M., Pollard, D., Robinson, J., Morino, I., Uchino, O., Hase, F., Blumenstock, T., Feist, D. G., Arnold, S. G., Strong, K., Mendonca, J., Kivi, R., Heikkinen, P., Iraci, L., Podolske, J., Hillyard, P. W., Kawakami, S., Dubey, M. K., Parker, H. A., Sepulveda, E., García, O. E., Te, Y., Jeseck, P., Gunson, M. R., Crisp, D., and Eldering, A.: Comparisons of the Orbiting Carbon Observatory-2 (OCO-2) XCO<sub>2</sub> measurements with TCCON, *Atmos. Meas. Tech.*, 10, 2209–2238, <https://doi.org/10.5194/amt-10-2209-2017>, 2017.
- Yokota, T., Yoshida, Y., Eguchi, N., Ota, Y., Tanaka, T., Watanabe, H., and Maksyutov, S.: Global concentrations of CO<sub>2</sub> and CH<sub>4</sub> retrieved from GOSAT: First preliminary results, *Sola*, 5, 160–163, 2009.